



NAVAL POSTGRADUATE SCHOOL

MONTEREY, CALIFORNIA

DISSERTATION

**DESIGN, FABRICATION, AND CHARACTERIZATION OF
A MICROELECTROMECHANICAL DIRECTIONAL
MICROPHONE**

by

Michael Touse

June 2011

Dissertation Supervisor:

Gamani Karunasiri

Approved for public release; distribution is unlimited

THIS PAGE INTENTIONALLY LEFT BLANK

REPORT DOCUMENTATION PAGE			Form Approved OMB No. 0704-0188	
Public reporting burden for this collection of information is estimated to average 1 hour per response, including the time for reviewing instruction, searching existing data sources, gathering and maintaining the data needed, and completing and reviewing the collection of information. Send comments regarding this burden estimate or any other aspect of this collection of information, including suggestions for reducing this burden, to Washington Headquarters Services, Directorate for Information Operations and Reports, 1215 Jefferson Davis Highway, Suite 1204, Arlington, Va 22202-4302, and to the Office of Management and Budget, Paperwork Reduction Project (0704-0188) Washington DC 20503.				
1. AGENCY USE ONLY (<i>Leave blank</i>)		2. REPORT DATE June 2011		3. REPORT TYPE AND DATES COVERED Dissertation
4. TITLE AND SUBTITLE Design, Fabrication, and Characterization of a Microelectromechanical Directional Microphone			5. FUNDING NUMBERS	
6. AUTHORS Touse, Michael				
7. PERFORMING ORGANIZATION NAME(S) AND ADDRESS(ES) Naval Postgraduate School Monterey CA 93943-5000			8. PERFORMING ORGANIZATION REPORT NUMBER	
9. SPONSORING/MONITORING AGENCY NAME(S) AND ADDRESS(ES)			10. SPONSORING/MONITORING AGENCY REPORT NUMBER	
11. SUPPLEMENTARY NOTES The views expressed in this thesis are those of the author and do not reflect the official policy or position of the Department of Defense or the U.S. Government. IRB Protocol Number:-----				
12a. DISTRIBUTION/AVAILABILITY STATEMENT Approved for public release; distribution is unlimited			12b. DISTRIBUTION CODE	
13. ABSTRACT(<i>maximum 200 words</i>) A series of micro-electromechanical system (MEMS) based devices for acoustic direction finding have been designed and fabricated which mimic the aural system of the <i>Ormia ochracea</i> fly and its extraordinary directional sensitivity. To overcome the minimal spatial separation between its ears, a flexible hinge mechanically couples the fly's two tympanic membranes. Because of this coupling, the phase differences due to the time difference of arrival (TDOA) are greatly amplified and sound source direction is determined with unparalleled speed and accuracy. This unique system allows the fly to acoustically locate crickets, which chirp with wavelengths two orders of magnitude greater than the dimensions of the hearing system. In this thesis, MEMS sensor design using finite element modeling and experimentation to characterize the physical phenomena that affect the performance will be described. Specific investigations reported include damping effects, device linearity to sound pressure, and the effects of various packaging schemes on device performance. Results include successful demonstrations of several directional sensors responsive to both sinusoidal and impulsive sources, an electronic readout scheme using capacitive comb fingers, an asymmetric design for dual frequency use, and devices effective into the ultrasonic range, all of which could ultimately contribute to a millimeter-scale device for sniper-location or a number of other defense applications.				
14. SUBJECT TERMS MEMS, Directional Microphones, Gunshot Detection, Coupled Oscillators			15. NUMBER OF PAGES 97	
			16. PRICE CODE	
17. SECURITY CLASSIFICATION OF REPORT Unclassified	18. SECURITY CLASSIFICATION OF THIS PAGE Unclassified	19. SECURITY CLASSIFICATION OF ABSTRACT Unclassified	20. LIMITATION OF ABSTRACT UU	

THIS PAGE INTENTIONALLY LEFT BLANK

Approved for public release; distribution is unlimited

**DESIGN, FABRICATION, AND CHARACTERIZATION OF A
MICROELECTROMECHANICAL DIRECTIONAL MICROPHONE**

Michael Touse

Lieutenant Commander, United States Navy

B.S. Physics, United States Naval Academy, 1997

M.S. Physics, Naval Postgraduate School, 2003

Submitted in partial fulfillment of the
requirements for the degree of

DOCTOR OF PHILOSOPHY IN APPLIED PHYSICS

from the

NAVAL POSTGRADUATE SCHOOL

June 2011

Author:	<hr/> Michael Touse	
Approved by:	<hr/> Gamani Karunasiri Professor of Physics Dissertation Supervisor	<hr/> Bruce Denardo Associate Professor of Physics
	<hr/> Douglas Fouts Professor of Electrical and Computer Engineering	<hr/> Dragoslav Grbovic Assistant Professor of Physics
	<hr/> Daphne Kapolka Senior Lecturer Physics Department	<hr/>
Approved by:	<hr/> Andres Larraza Chair, Department of Physics	
Approved by:	<hr/> Doug Moses Vice Provost for Academic Affairs	

THIS PAGE INTENTIONALLY LEFT BLANK

ABSTRACT

A series of micro-electromechanical system (MEMS) based devices for acoustic direction finding have been designed and fabricated which mimic the aural system of the *Ormia ochracea* fly and its extraordinary directional sensitivity. To overcome the minimal spatial separation between its ears, a flexible hinge mechanically couples the fly's two tympanic membranes. Because of this coupling, the phase differences due to the time difference of arrival (TDOA) are greatly amplified and sound source direction is determined with unparalleled speed and accuracy. This unique system allows the fly to acoustically locate crickets, which chirp with wavelengths two orders of magnitude greater than the dimensions of the hearing system. In this thesis, MEMS sensor design using finite element modeling and experimentation to characterize the physical phenomena that affect the performance will be described. Specific investigations reported include damping effects, device linearity to sound pressure, and the effects of various packaging schemes on device performance. Results include successful demonstrations of several directional sensors responsive to both sinusoidal and impulsive sources, an electronic readout scheme using capacitive comb fingers, an asymmetric design for dual frequency use, and devices effective into the ultrasonic range, all of which could ultimately contribute to a millimeter-scale device for sniper-location or a number of other defense applications.

THIS PAGE INTENTIONALLY LEFT BLANK

Table of Contents

1	Introduction	1
2	Biological Background	3
3	Structure	13
3.1	Damping	18
3.2	Comb Fingers	20
3.3	Finite Element Modeling	22
3.4	Pressure Gradients	24
3.5	Chip Layout	27
4	Fabrication	31
4.1	Fabrication Results	34
5	Measurement Setup	37
5.1	Laser Vibrometry	39
5.2	Readout	42
5.3	Lock-in Amplifier	44
6	Results	47
6.1	Frequency Response	47
6.2	Directionality	48
6.3	Linearity	49
6.4	Damping	51
6.5	Perforated Wings	56
6.6	Packaging Effects	59
6.7	Impulsive Sources	61
7	Dual Frequency Sensor	65

8 Conclusion	69
Appendix	71
List of References	73
Initial Distribution List	77

List of Figures

Figure 2.1	Photo of <i>Ormia ochracea</i>	3
Figure 2.2	Diagram of ITD and ILD	4
Figure 2.3	Hearing system of <i>Ormia ochracea</i>	6
Figure 2.4	Mechanical model of <i>Ormia ochracea</i>	7
Figure 2.5	Bending mode	8
Figure 2.6	Rocking mode	8
Figure 2.7	Frequency response of mechanical model	9
Figure 2.8	Time-domain response of mechanical model	10
Figure 3.1	Device design - top	14
Figure 3.2	Device design - top	15
Figure 3.3	Geometry definition	16
Figure 3.4	Comb finger design	21
Figure 3.5	FEM frequency response	24
Figure 3.6	Device design - bottom	25
Figure 3.7	Pressure-gradient directional response	26
Figure 3.8	Finite Element Model rocking mode response	27
Figure 3.9	Diagram of trenched device	29
Figure 4.1	Fabrication steps - Substrate	31
Figure 4.2	Fabrication steps - Pad Metal Deposition	32

Figure 4.3	Fabrication steps - Etching	32
Figure 4.4	Fabrication steps - Substrate trenching	33
Figure 4.5	Fabrication steps - SiO ₂ etch/release	33
Figure 4.6	Fabrication steps - Blanket metal deposition	34
Figure 4.7	Device photograph and comb finger inset	35
Figure 4.8	SEM image of comb fingers	35
Figure 4.9	SEM image of fabricated chip	36
Figure 4.10	Photo of trenched device	36
Figure 5.1	Mounted device	37
Figure 5.2	SOIC packaging	38
Figure 5.3	Laboratory setup	39
Figure 5.4	Speaker directionality	40
Figure 5.5	Polytec vibrometer	41
Figure 5.6	Simplified MS3110 diagram	43
Figure 5.7	Diagram of device electronics	43
Figure 5.8	Electronic readout results	45
Figure 5.9	Lock-In Amplifier setup	45
Figure 6.1	Combined frequency response of device	47
Figure 6.2	Directional frequency response of symmetric device	48
Figure 6.3	Directional response of symmetric device	49
Figure 6.4	Device linearity	50
Figure 6.5	Transient response at high and low power	50
Figure 6.6	Frequency response of comb fingers	52
Figure 6.7	Normalized rise-time comparison	53

Figure 6.8	Absolute transient response	53
Figure 6.9	Effect of doubling comb fingers	56
Figure 6.10	SEM image of perforations	57
Figure 6.11	Frequency response of perforated vs. solid wings	58
Figure 6.12	SEM images of device with with 2 μm perforations.	59
Figure 6.13	Frequency response of larger perforations	60
Figure 6.14	Device response for various package dimensions	61
Figure 6.15	Gunshot response by angle	62
Figure 6.16	Amplitude versus gunshot angle	63
Figure 7.1	Asymmetric footprint	65
Figure 7.2	Simulated frequency response of asymmetric device FEM	66
Figure 7.3	FEM directional response of asymmetric device	67
Figure 7.4	Asymmetric device photograph	67
Figure 7.5	Asymmetric frequency response by angle	68

THIS PAGE INTENTIONALLY LEFT BLANK

List of Tables

Table 3.1	Dimensions of fabricated device shown in Figure 4.7.	28
Table 6.1	Device dimensions used to compare effects of comb fingers on damping	51
Table 6.2	Comparison of devices with and without comb fingers	52
Table 6.3	Comparison of two devices with identical dimensions except that one (3C+) has more comb fingers than the other.	54
Table 6.4	Comparison of three devices with identical dimensions except for the number of comb fingers attached.	55
Table A.1	Generation 4	71
Table A.2	Generation 5 - Bowtie shape, 125 fingers/side and 2 μm pitch.	71
Table A.3	Generation 6 - Bowtie shape, 125 fingers/side and 2 μm pitch.	72
Table A.4	Generation 8 - 10 μm layer. All bowtie shape.	72

THIS PAGE INTENTIONALLY LEFT BLANK

List of Acronyms and Abbreviations

AC	Alternating Current
ADC	Analog to Digital Converter
CAD	Computer Aided Design
CNS	Central Nervous System
DC	Direct Current
DIP	Dual Inline Package
DRIE	Deep Reactive Ion Etching
EEPROM	Electrically Erasable Programmable Read-Only Memory
FEM	Finite Element Model
FFT	Fast Fourier Transform
FWHM	Full Width at Half Maximum
HRTF	Head Related Transfer Function
IC	Integrated Circuit
ICP	Inductively Coupled Plasma
IID	Interaural Intensity Difference
ILD	Interaural Level Difference
ITD	Interaural Time Difference
LDV	Laser Doppler Vibrometry
LIA	Lock In Amplifier
MEMS	Microelectromechanical Systems
PGA	Pin Grid Array
PML	Perfectly Matched Layer
PSG	Phosphosilicate Glass
PSOIC	Plastic Small Outline Integrated Circuit
PTM	Prosternal Tympanal Membrane
RIE	Reactive Ion Etching
RMS	Root Mean Squared
SOC	System-On-Chip
SOIC	Small Outline Integrated Circuit
SOIMUMPS	Silicon-On-Insulator Multi-User MEMS Process
SPL	Sound Pressure Level
VCSEL	Vertical Cavity Surface Emitting Laser

THIS PAGE INTENTIONALLY LEFT BLANK

Acknowledgements

I would first like to thank the National Consortium for MASINT Research for their generous financial support in bringing this project to its current state and providing the basis to eventually transition this research into an operational system. Additionally I would like to thank the Space and Naval Warfare Systems Command, San Diego, for their support through the SPAWAR student fellowship.

A number of students have conducted research as part of this project and all deserve a great deal of credit for providing a solid foundation on which to build, for providing individual elements of our current understanding, and for helping me better recognize the pieces that still need work. Specifically, I thank Tim Shivok for his previous work and Norbahrin Muamad, Stephen Harrison, Kursad Simsek, and Dimitrios Grevenitis for their work during the course of my research. Also, thanks to Rich Downey, John Roth, Darren Davis, and Choon Wee for keeping me honest as I try to turn over all the details of the research - I am glad to know the project is in very good hands.

Jay Adeff, Sam Barone, George Jaksha, and Kerry Yarber deserve an enormous amount of credit for the research that went into this dissertation as they continually find solutions to our myriad lab difficulties, not to mention their help with a relatively seamless transition into our new lab. Our interns, Jeffrey Catterlin and Jeremy Blalock, have also been a tremendous help to this project and I extend my thanks and wish them the best of luck.

I would also like to thank the Physics Department's PhD committee and my dissertation committee for their encouragement and patience through the entire process as well as that from my fellow PhD students (especially during qualifying exams).

It would not be possible to adequately thank my dissertation supervisor, Professor Gamani Karunasiri, for his role in getting me through this program. His ability to provide perspective and frame both the PhD process and research into something manageable is simply astounding and I will always be grateful.

Finally, I want to thank my family for their patience and encouragement through all my studying and traveling throughout this entire tour. Were it not for the loving family cheering me each step of the way, I certainly would not have made it this far.

THIS PAGE INTENTIONALLY LEFT BLANK

CHAPTER 1:

Introduction

Acoustic direction-finding has been a problem as long as animals have roamed the Earth. The sounds made by predators and prey travel past the head of a large animal. At any instant the two ears sense the pressure difference between them because each ear is located at a different phase angle within the sound's wavelength. If the pressure change at one ear leads the other, then the ear sensing the leading signal is closer to the source. If the wavelength is very long, however, the ears sense a nearly identical pressure and it sounds as if the source is directly in front of or behind the head. By turning its head the animal can try to induce a phase difference between its ears, but if that fails it will look for other cues. Human hearing is naturally tuned to the wavelengths that are roughly the same order of magnitude as the distance between our ears so we can effectively detect sound source direction.

Small animals, insects in particular, generally do not rely heavily on acoustic orientation because the wavelength of most acoustic cues are much longer than the separation between the insect's ears[1]. In 1974 and 1975, a study was conducted that determined a particular species of parasitoid fly, the *Ormia ochracea*, could locate singing male crickets acoustically[2]. Gravid female flies turn towards a singing cricket, approach it, and deposit larvae on or near the host cricket. These larvae then burrow into the cricket and kill it within 10 days[3]. The remarkable part of this biological system is that the *Ormia ochracea* has a tympanal (eardrum) separation of less than 0.5mm versus the wavelength of a cricket chirp, which is nearly 7 cm. This equates to an interaural time difference (ITD) of, at most, $1.5 \mu s$, which is too short to be detected by the fly[4]. Likewise, the maximum geometric phase difference is less than one percent of the wavelength of interest, making the interaural level difference (ILD) equally imperceptible. Yet despite these biological challenges, the *Ormiine* hearing system can consistently detect sound source azimuth differences of less than 2° [5].

The mechanism for achieving this remarkable directional sensitivity is through the mechanical coupling of the fly's two tympana[6]. Instead of using two independent sensors as with most acoustic direction-finding systems, the *Ormia ochracea*'s eardrums are joined by a semi-rigid intertympanal bridge. While the incident sound drives the two tympana nearly in-phase with each other, the mechanical coupling introduces an out-of-phase component that opposes the acoustic driving pressure. These opposing forces effectively slow the response of the contralat-

eral tympanum (the side farthest from the source) and amplify the ITD by a factor of twenty or more. A full explanation of the mechanical amplification of both the ITD and ILD was first presented in [6] and [7].

The potential military applications for sensitive acoustic direction-finding systems are endless and are continually under development. Of particular interest in the current military environment is the use of sound to help identify the direction of sniper fire. Because the intended targets for sniper fire are generally individual troops moving on foot, the intended user for such a system would be individual soldiers who are already weighed down with large amounts of protective gear and weapons. For this reason, an acoustic sniper detection system must be as small and light as possible for it to be useful. Other potential applications of acoustic direction-finding equipment include their use as a remote sensor for intelligence purposes or in the civilian sector to help people with hearing aids be able to better ascertain direction in noisy environments. The medical community has also expressed interest in monitoring troop exposure to overpressures from large blasts to study Traumatic Brain Injury.

The ultimate goal of this research is to develop a millimeter-scale device to be used as an acoustic direction finding system. Because the *Ormiine* hearing system so effectively uses miniscule interaural cues, it has motivated a number of studies which emulate the structure to create miniature directional sound receivers[8, 9, 10, 11, 12]. The research presented here, however, uses greatly simplified fabrication and readout techniques, and investigates the individual components of these particular devices.

The presentation of this material begins with an explanation of the *Ormiine* hearing system and how that system determines sound direction. Then the specific theory of how a synthetic device fabricated to emulate that system should react, including each of the various design features that have been used. The fabrication process is described next, followed by the laboratory equipment description. The experimental results are then presented including a detailed analysis of several of the device's features and their impact on the response characteristics, as well as a design variation to make a dual band sensor.

CHAPTER 2:

Biological Background

The hearing system of the *Ormia ochracea* (see Figure 2.1) is remarkable mainly due to its acute directional sensitivity to sounds with such long wavelengths (compared to the dimensions of the fly's hearing system). In humans, the direction of low frequency sources ($f < 500$ Hz) is determined primarily by sensing the interaural time difference (ITD)[13, 14]. The difference in arrival times for a human ranges from zero when the source is straight ahead, to several hundreds of microseconds when the source is directly to one side. Given the minimum ITD detectable by humans is approximately $10 \mu s$ [15], the minimum angular resolution in humans is approximately 1° . At higher frequencies, humans have an even greater advantage as the head creates an acoustical shadow at the contralateral ear and causes an interaural intensity difference (IID) between the two ears.



Figure 2.1: Photo of *Ormia ochracea*. From [16]

Smaller animals, like insects, have much smaller interaural differences due to their small size. The *Ormia ochracea* has an interaural separation of only $520 \mu m$ which yields a maximal interaural time difference of $2 \mu s$ [7]. Like humans, smaller animals that have been studied

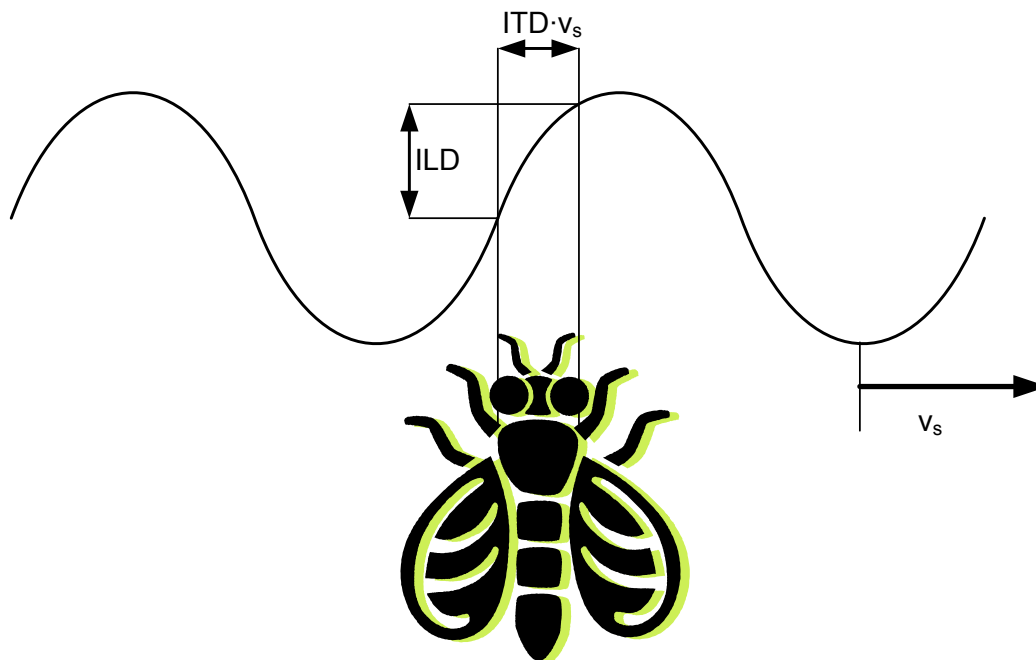


Figure 2.2: Illustration of interaural level difference (ILD) and interaural time difference (ITD). Note that in this illustration the wavelength is comparable to the dimensions of the fly.

(birds, cats, insects) can only perceive stimulus time differences of $10 \mu s$ or greater[17], making the interaural time differences inadequate for acoustic sound source location.

For wavelengths that are comparable to the distance between the two ears, in lieu of detecting the time difference between the two ears, an organism could detect a phase, or amplitude difference as in Figure 2.2. If the wavelength is much longer than the distance between the ears, however, this interaural level difference (ILD) is imperceptible since the pressure level at the two ears is essentially in-phase. This is the case with the *Ormia ochracea* because the system is located far from the source and is much smaller than the wavelength of interest. It is, therefore, appropriate to approximate the incident sound as a plane wave with no spreading loss and essentially no attenuation between the ears due to the small size.

The first observations of acoustic orientation by the *Ormia ochracea* occurred in 1974 and 1975[2]. Using two speakers in a small chamber, gravid (larvae-carrying) female *Ormine* flies were attracted to the speaker that was playing a synthetic reproduction of the song of the *Gryllus*

integer cricket (whose song is typically around 5 kHz). In nature, these flies acoustically orient themselves and deposit their larvae on or near singing crickets[3]. Within ten days, the larvae feed on and emerge from the host. In some cases, satellite crickets (silent male crickets that position themselves near singing ones in hopes of mating with a female responding to a song) have also been found parasitized by the larvae.

In every case during the study, the flies chose the speaker playing the cricket song over the other (control) speaker, which played sounds of equal intensity and in the same frequency range. After locating the correct speaker, the flies walked around the speaker and the dead cricket mounted there, depositing its living larvae. Later studies also showed that the flies respond to the songs of the *Gryllus rubens* and, to a lesser extent (likely due to its lower frequency of 3 kHz), the *Scapteriscus acletus*[18].

Plagued with the problems identified above of having to measure minute interaural time and sound pressure level (SPL) differences, the female *O. ochracea* has evolved with a tympanal hearing system similar to insects like katydids, grasshoppers, moths, cicadas, and mantises. This is a very unique feature among flies, as most use individual antennae-like sensors (called Johnson's organs) to detect low-frequency air movement. The *Ormiine* tympanal system is resonant in the 4–8 kHz range, and the nervous system receptors are well matched to include the same frequencies, which are characteristic of the host[19]. The fly also exhibits some sensitivity in the ultrasonic range, which may help with predator avoidance[3].

The hearing system of the *Ormia ochracea*, shown in Figure 2.3, is located below the base of the neck and above the prothoracic coxae (the base of its front legs); it spans up to 80% of the width of the body, which places the extreme edges of the system beyond the outer edge of the coxae and near the outer perimeter of the head[20]. Compared to atympanal species within the same (*Tachinidae*) family, the *O. Ochracea* has an enlarged probasisternum that acts as a frame around the entire organ and to which the prosternal tympanal membranes (PTM, or tympana) are attached. It also has a unique anisotropic corrugation in the tympana that directs the mechanical response of the tympana to the actual sensory organs located in the presternum.

While comparable species contain presterna that are medially concentrated near the neck, the *Ormiini* (all of which are tympanates) have a presternum that splits and each branch runs laterally outward along one half of the PTM. The two branches of this forked presternum terminate at the tympanal pits, which are connected through the PTM to the sensory organs (bulbae acusticae) that lie inside the air-filled prosternal chamber. The combination of a semi-rigid prester-

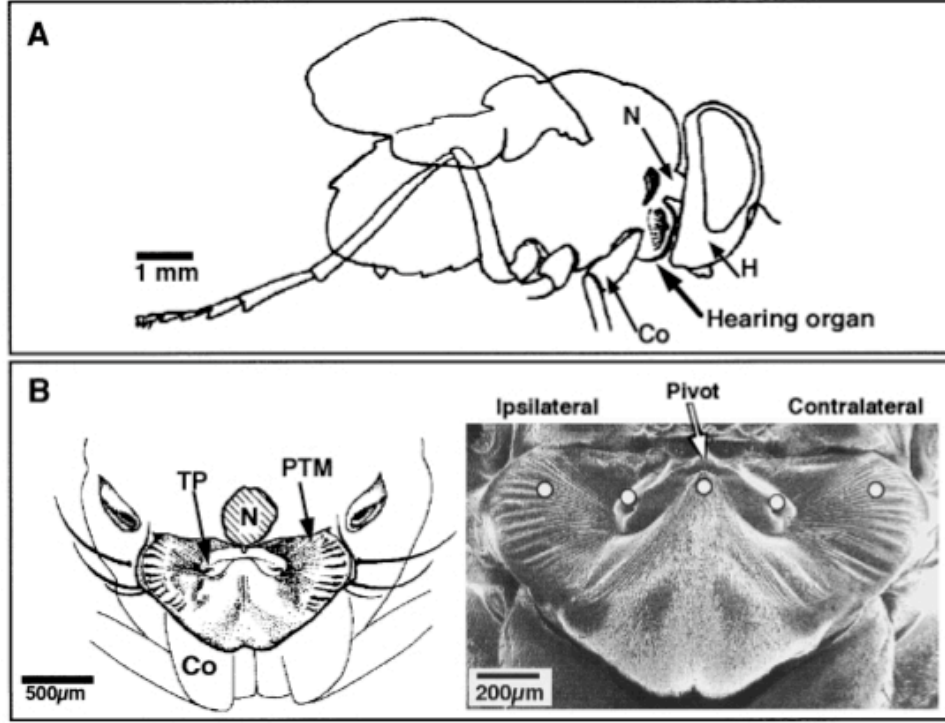


Figure 2.3: Hearing system of *Ormia ochracea* by Miles, et al. Reprinted with permission from [6]. Copyright 1995, Acoustical Society of America.

num and its connection to two independent sensory organs through intact tympana provide the primary mechanism for the directional hearing of the *Ormiine* flies[3].

In order to better understand how these particular components allow for such precise long-wavelength direction finding, the hearing system of the *Ormia ochracea* has been modeled as two identical and opposing damped cantilevers as seen in Figure 2.4[6]. These represent the two branches of the presternum where the properties of the PTM are modeled by the spring and damping constants (k_1 , c_1 and k_2 , c_2). The two cantilevers are coupled together by a spring with a different stiffness and damping coefficient, k_3 and c_3 , respectively. Incident sound is then simply a sinusoidal driving force acting normally on the cantilevers.

In the limit of zero coupling ($k_3 \rightarrow 0$), the model would clearly be two cantilevers driven in-phase (due to their proximity to each other compared to the wavelength), with amplitudes directly dependent on the external force. Conversely, in the limit of infinite coupling stiffness ($k_3 \rightarrow \infty$), the system becomes a lever with the fulcrum in the middle of the device. The force on the ipsilateral side is then transmitted directly to the contralateral side but in a direction

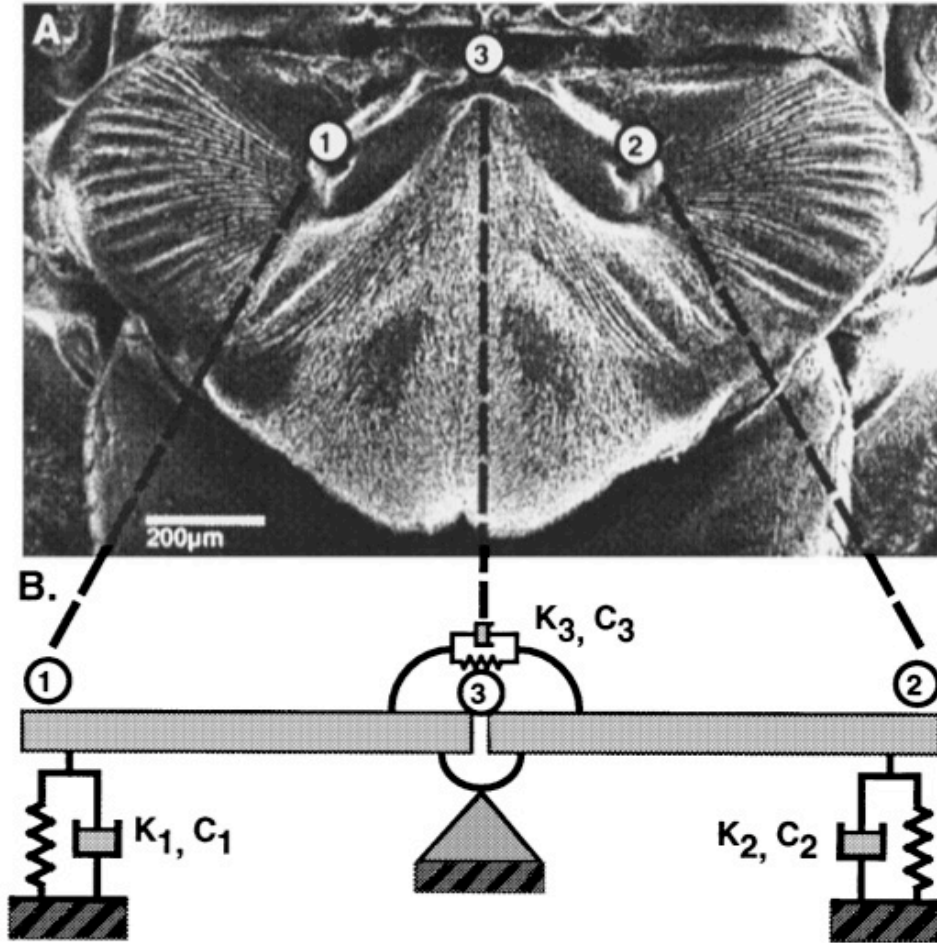


Figure 2.4: Fly and proposed mechanical model. Reprinted with permission from [6]. Copyright 1995, Acoustical Society of America.

that opposes the external force and makes the two cantilevers oscillate out-of-phase. Given a finite coupling stiffness, the overall motion is a linear combination of these two extremes. The bending (in-phase) mode, shown in Figure 2.5, is driven strictly by the *sum* of pressures on the two sides and is mostly dependent on the stiffness of the coupling spring. The rocking (out-of-phase) mode, shown in Figure 2.6, is excited due to a *difference* in pressure on the two wings and is primarily affected by the spring constant of the individual cantilevers.

As previously discussed, in a long-wavelength sensor, the two oscillators are in such close proximity compared to the incident wavelength that the external force on the two sides can be generally considered to be in-phase and of comparable amplitude. As a result, the difference in the instantaneous pressures is much smaller than the sum, making the bending mode much

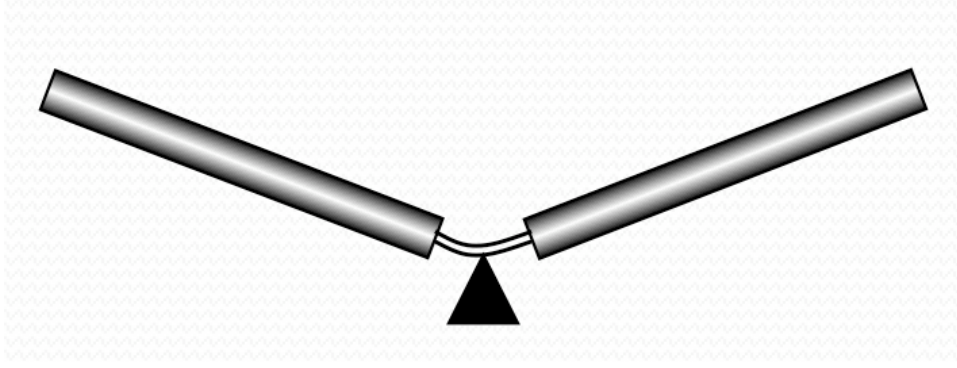


Figure 2.5: Simplified mechanical model showing bending mode of device.

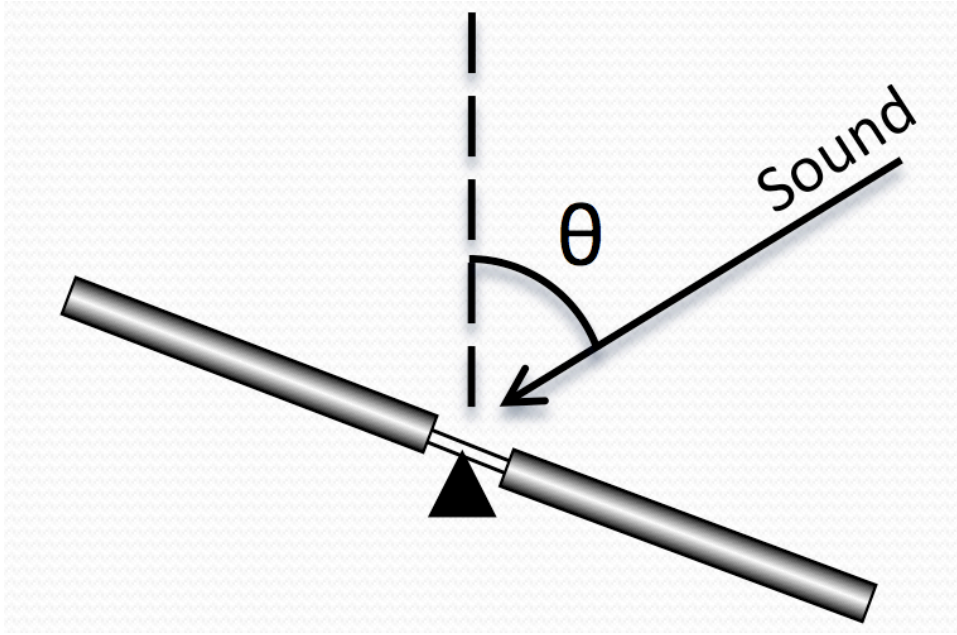


Figure 2.6: Simplified mechanical model showing rocking mode of device.

more pronounced than the rocking mode. Because the rocking and bending modes are governed by different spring constants, the resonances of the two modes occur at different frequencies as can be seen by Figure 2.7.

To understand the reason for the sensor's directional dependence, let the interaural time difference (τ) of a plane wave incident on the two wings be given by $d \sin \theta / v_s$ (where d is the lateral separation of the two tympana, θ is the angle of incidence from normal, and v_s is the speed of sound). If the angular frequency of the incident sound wave is ω , then the corresponding

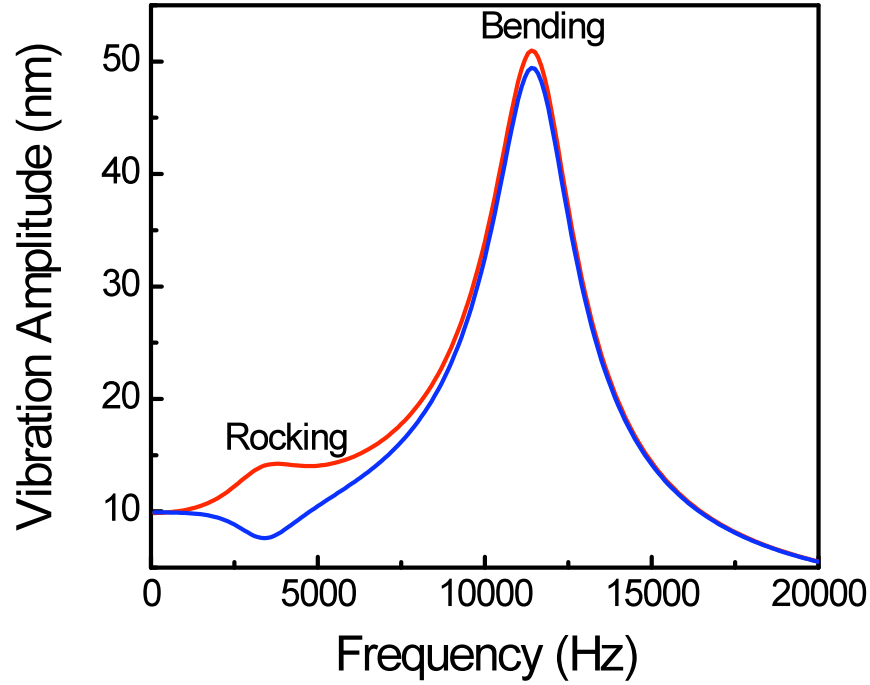


Figure 2.7: Theoretical frequency response of each side of the simplified mechanical model shown in Figure 2.4. From[21].

phase difference from the midpoint is given by $2\phi \equiv \omega\tau$. Because the dimensions of the device are small compared to the wavelength at resonance, the pressure amplitude is nearly constant across the device which means the rocking mode is almost entirely driven by the phase difference, $\omega\tau$ [6]. The amplitudes of the rocking, A_r , and bending, A_b , modes are then proportional to the difference and sum of the sound pressure on the two wings, which can be written as

$$\begin{aligned} A_r &\propto sP_0(e^{i(\omega\tau/2)} - e^{-i(\omega\tau/2)}) \\ A_b &\propto sP_0(e^{i(\omega\tau/2)} + e^{-i(\omega\tau/2)}) \end{aligned} \quad (2.1)$$

and, using $\phi = \omega\tau/2$, be simplified as

$$\begin{aligned} A_r &\propto sP_0 \cdot \sin \phi \\ A_b &\propto sP_0 \cdot \cos \phi \end{aligned} \quad (2.2)$$

where s is the area of each wing, and P_0 is the incident acoustic pressure amplitude. In the long-wavelength limit, however, the phase difference between the two sides becomes only a few degrees, and Equations (2.2) can be simplified using the standard small-angle approximations to obtain the directional dependence of the rocking and bending amplitudes, given as

$$\begin{aligned} A_r &\propto (\omega d/v_s) s P_0 \sin \theta \\ A_b &\propto s P_0 \end{aligned} \quad (2.3)$$

Stated more plainly in physical terms, if the sound field is normally incident on the device, assuming the field can be approximated as a plane wave, the instantaneous force on the two sides of the device will be identical and no rocking mode will be induced. As the sound source is moved to one side of the device, however, the instantaneous force on the two sides will start to differ by an amount proportional to the sine of the angle of incidence as seen in Equations (2.3).

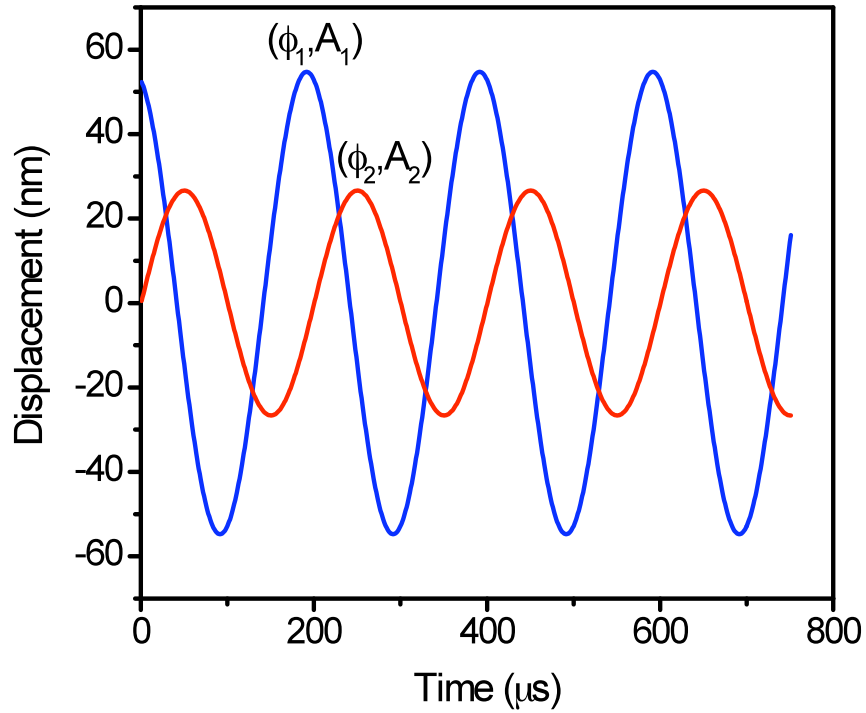


Figure 2.8: Theoretical steady-state response of the simplified mechanical model. From [21]

While this type of structure allows a significant advantage to the fly by inducing a measurable difference in response amplitude that depends on the angle of incidence, it also greatly increases the response time delay as seen both theoretically in the model (shown in Figure 2.8)[21], and experimentally in the actual fly's sensing system[6]. Further experimentation has shown that the mechanical system itself multiplies the ITD of $1.5 \mu s$ to a mechanical response time-difference of more than $50 \mu s$, a time-scale that is certainly encodable with observed neuronal systems[7].

Sound source direction might be detectable simply by using the increased time and amplitude differences delivered by the mechanical system, but it is further aided by the nervous system. It had been previously observed in locusts that the latency between the mechanical response and the signal arrival at the central nervous system (CNS) was highly dependent on amplitude[17], increasing the physical time of sound arrival by a factor of up to 1000 by the time the signal reached the CNS. Similarly, in the *Ormia ochracea*, the arrival-time difference of approximately $2 \mu s$ is magnified to $320 \mu s$ when the nervous system latency is included.

Finally, it bears mentioning that the *Ormia ochracea* has shown an ability to differentiate sound source elevation as well as azimuth[22]. In that experiment, tethered flies were able to differentiate synthetic cricket chirps incident from 42.5° above horizontal from those 42.5° below horizontal. Because of the large angular separation of the two experimental sources, it is reasonable that the fly might be able to use its Head Related Transfer Function (HRTF), though the exact mechanism for this ability is still unknown.

Given the increased amplitude and phase difference between the two tympanal responses, the fly is able to sense these differences and convert them into an incidence angle. With the understanding of the mechanical system used by the *Ormiine* fly, the next step in the research was to develop a device that emulates it both in size and sensitivity.

THIS PAGE INTENTIONALLY LEFT BLANK

CHAPTER 3:

Structure

A number of micro-electromechanical systems (MEMS) based devices have been developed that emulate the fly's hearing system. For example, Miles, et al.[9], employed interdigitated diffracting gratings combined with a vertical cavity surface emitting laser (VCSEL) and photodiode array for measuring vibration amplitudes interferometrically. One group used a capacitive diaphragm and backplate scheme, similar to that used in conventional electrostatic microphones[23], and another used a Fabry-Perot interferometer made from a superluminescent diode and a Mylar diaphragm that acts as the tympanum[24].

In order to simplify the entire system to allow the smallest possible package, the presented devices are fabricated using standard semiconductor and silicon device processing technology, available through MEMSCAP, INC., which fabricates micro-electromechanical systems (MEMS) in small quantities by sharing wafer-space among multiple users. This patented process is called MUMPS (Multi-User MEMS Processes). Their Silicon-on-Insulator process, SOIMUMPS, is the specific process used for all the designs presented here.

The SOIMUMPS process involves using either a $10\ \mu m$ or $25\ \mu m$ device layer of doped (conductive) single-crystal silicon atop a $1\ \mu m$ insulating layer of silicon dioxide (SiO_2). This entire structure is created on a $400\ \mu m$ silicon substrate. The process allows for etching both the device layer and the substrate layer, as well as metallization of the top-side of either layer.

Given the constraints of this process, the goal was to develop a structure that roughly matched the *Ormiine* hearing structure both in size and performance. In order to achieve this, the designs needed to maximize the displacement amplitude and maintain the two independent, but coupled, modes of oscillation. The devices developed in [21] were the first iteration and used a system of opposing cantilevers made from a $7\ \mu m$ device layer of alternating Polysilicon and SiO_2 with very narrow ($14\ \mu m$) legs connecting the two *wings* (tympana) to the surrounding stationary device layer. The dimensions of the legs allow them to act as a torsional spring whose stiffness (along with the mass of the tympana) govern the rocking mode of the device. Because the device layer is thin ($10\ \mu m$), it can bend in the middle as well. In these first iterations, the bending mode was only governed by the dimensions of the wings. In order to increase the coupling between the two modes, it was important to reduce the separation between the two resonances

in the frequency domain. This was accomplished by removing a portion of the device layer along the central rotational axis as seen in Figure 3.1. This reduces the effective spring constant of the bending mode while leaving the rocking mode unaffected. The other way to control the bending stiffness is to reduce the width of the bridge, resulting in a bowtie-shaped structure as seen in Figure 3.2. While not rigorously verified experimentally, the bowtie-shaped devices seemed to exhibit a slightly increased mechanical sensitivity, so the latest iterations of device designs were of the bowtie type.

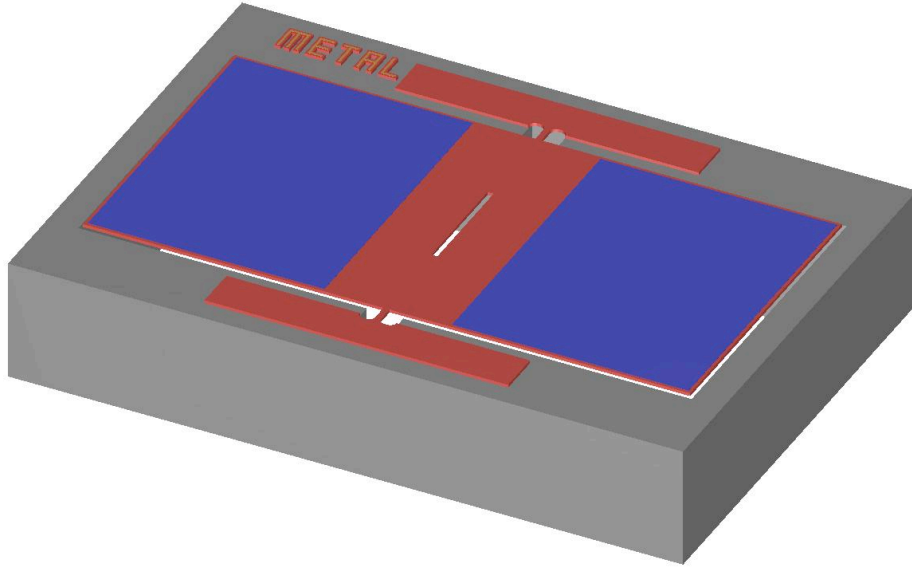


Figure 3.1: Designed rectangular device structure.

This structure differs from the initial mechanical model used to describe the fly’s hearing system in that there are no springs attaching the ends of the cantilevers to the fixed substrate. The effects of this difference can be seen by evaluating the equations of motion as in [25]. Beginning with the Lagrangian (excluding damping for now)

$$\mathcal{L} = T - V \quad (3.1)$$

where \mathcal{L} is the Lagrangian, T is the kinetic energy of the device, and V is its potential energy stored in the torsional (legs) and bending (bridge) springs.

To find the energy terms, the rotational inertia of the device is used. In that case the kinetic and

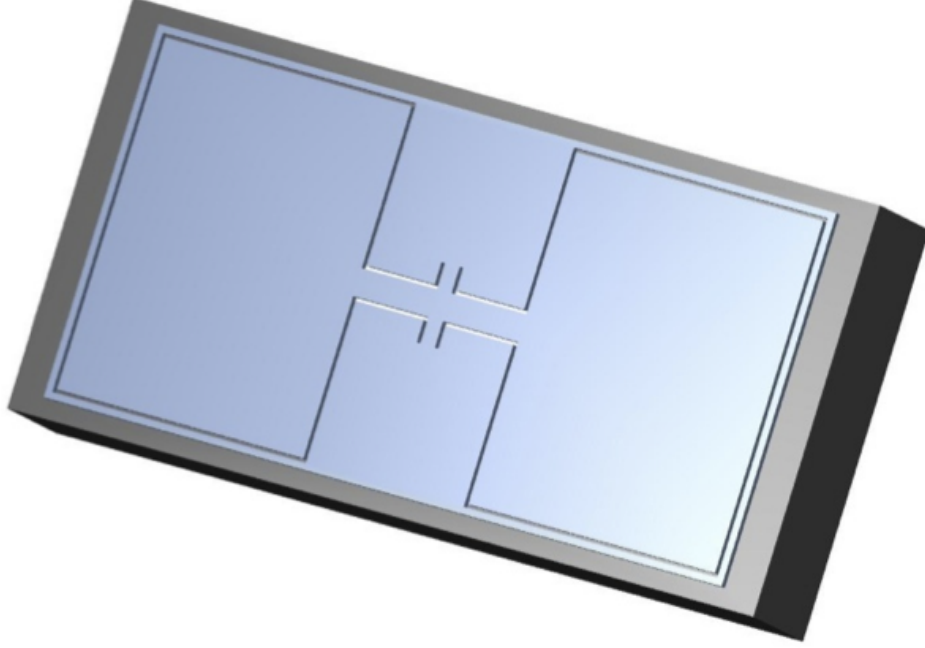


Figure 3.2: Designed bowtie-shaped structure.

potential energies are found in terms of the moment of inertia (I), and angular displacements of the two sides (θ_1 and θ_2). The geometry is shown in Figure 3.3. The kinetic energy is given by

$$T = \frac{I\dot{\theta}_1^2}{2} + \frac{I\dot{\theta}_2^2}{2} \quad (3.2)$$

In general, the potential energy stored in a torsional spring or cantilever is given by

$$V = \frac{k\theta^2}{2} \quad (3.3)$$

where k is the torsional spring constant. However, the presented devices have been designed with two different spring constants. The legs connecting the device to the surrounding substrate act as a torsional spring, each with stiffness k_{leg} , while the bridge connecting the two wings acts as a standard cantilever with spring constant k_{bridge} .

To understand the forces influenced by k_{leg} , one can see that if a single cantilever were anchored at the sides as with the presented device designs, the torsional restoring force from each leg would simply follow a Hooke's Law relationship: $F_{leg} = -k_{leg}\theta$. Adding the opposing can-

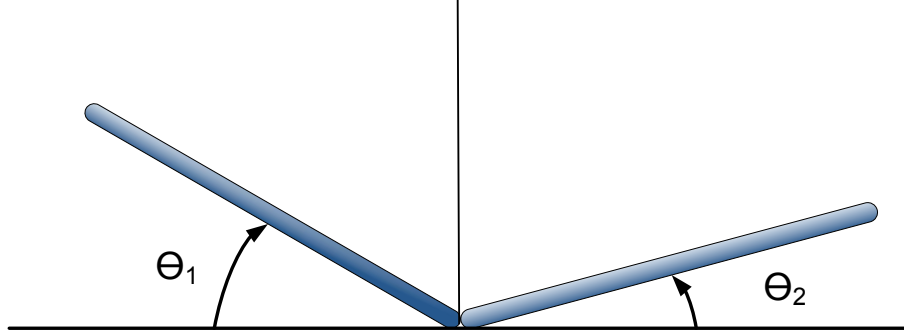


Figure 3.3: Simplified diagram of two wings to show the definition of the terms used in the theoretical derivation. Note that θ is positive when the associated wing is displaced vertically upward, away from the substrate.

tilt, however, affects this force by increasing or decreasing the shear experienced through the leg. If θ_1 and θ_2 are defined to both be positive when displaced vertically upward as seen in Figure 3.3, then if the two sides are displaced in opposite directions by an angle θ , the angle subtended by the legs is also θ . From this reasoning, one can see that each wing contributes half of the total angular displacement of the legs and

$$\theta_{leg} = \frac{\theta_1 - \theta_2}{2} \quad (3.4)$$

In the case of opposite displacement mentioned above, then $\theta = \theta_1 = -\theta_2$, and the total angle subtended by the leg is $\theta_{leg} = (1/2)(\theta - (-\theta)) = \theta$. Conversely, if both wings are displaced upward so that $\theta = \theta_1 = \theta_2$, there would be no shear on the legs and $\theta_{leg} = (1/2)(\theta_1 - \theta_2) = 0$, confirming the accuracy of Equation (3.4). A similar analysis for k_{bridge} is more straightforward. If one wing is deflected upward by an angle, θ , it experiences a force of $F_{bridge} = -k_{bridge}\theta/2$. The stiffness, k_{bridge} is defined as if the device were just one-half of the actual device (or just one wing), so when this is translated to a complete (two wing) device it effectively makes the spring twice as long, reducing the total stiffness by one-half. If the other wing is then deflected equally in the same direction, the restoring force *on the first wing* is doubled; namely $F_{bridge} =$

$-k_{bridge}\theta$. It can also be understood if one imagines the two sides displaced equally in opposite directions in which case the bridge would not bend at all so $F_{bridge} = -k_{bridge}(\theta - \theta)/2 = 0$. This translates into a general relationship for the bridge spring such that

$$\theta_{bridge} = \frac{\theta_1 + \theta_2}{2} \quad (3.5)$$

Applying these to Equation (3.3), we have

$$V = k_{leg} \left(\frac{\theta_1 - \theta_2}{2} \right)^2 + k_{bridge} \left(\frac{\theta_1 + \theta_2}{2} \right)^2 \quad (3.6)$$

which can be combined with Equations 3.1 and 3.2 to give the Lagrangian as

$$\mathcal{L} = \frac{I(\dot{\theta}_1 + \dot{\theta}_2)^2}{2} - k_{leg} \left(\frac{\theta_1 - \theta_2}{2} \right)^2 - k_{bridge} \left(\frac{\theta_1 + \theta_2}{2} \right)^2 \quad (3.7)$$

Given Lagrangian's equation of motion

$$\frac{d}{dt} \left(\frac{\partial \mathcal{L}}{\partial \dot{\theta}_i} \right) = \frac{\partial \mathcal{L}}{\partial \theta_i} \quad (3.8)$$

the next step is to solve for the individual differentials. Giving

$$\begin{aligned} \frac{\partial \mathcal{L}}{\partial \theta_1} &= -k_{leg} \left(\frac{\theta_1 - \theta_2}{2} \right) - k_{bridge} \left(\frac{\theta_1 + \theta_2}{2} \right) \\ \frac{\partial \mathcal{L}}{\partial \theta_2} &= k_{leg} \left(\frac{\theta_1 - \theta_2}{2} \right) - k_{bridge} \left(\frac{\theta_1 + \theta_2}{2} \right) \\ \frac{\partial \mathcal{L}}{\partial \dot{\theta}_1} &= I\dot{\theta}_1 \\ \frac{\partial \mathcal{L}}{\partial \dot{\theta}_2} &= I\dot{\theta}_2 \\ \frac{d}{dt} \left(\frac{\partial \mathcal{L}}{\partial \dot{\theta}_1} \right) &= I\ddot{\theta}_1 \\ \frac{d}{dt} \left(\frac{\partial \mathcal{L}}{\partial \dot{\theta}_2} \right) &= I\ddot{\theta}_2 \end{aligned} \quad (3.9)$$

The equations of motion are then

$$\begin{aligned} I\ddot{\theta}_1 &= -k_{leg}\left(\frac{\theta_1 - \theta_2}{2}\right) - k_{bridge}\left(\frac{\theta_1 + \theta_2}{2}\right) \\ I\ddot{\theta}_2 &= k_{leg}\left(\frac{\theta_1 - \theta_2}{2}\right) - k_{bridge}\left(\frac{\theta_1 + \theta_2}{2}\right) \end{aligned} \quad (3.10)$$

Solving for the motion at the two normal modes defined by

$$\begin{aligned} \text{Rocking mode:} \quad \theta_1 &= -\theta_2 \\ \text{Bending mode:} \quad \theta_1 &= \theta_2 \end{aligned}$$

we have

$$\begin{aligned} \ddot{\theta}_r &= \pm \frac{k_{leg}}{I} \theta_r \\ \ddot{\theta}_b &= \frac{k_{bridge}}{I} \theta_b \end{aligned}$$

so

$$\begin{aligned} \theta_r(t) &= \theta_r e^{i\omega_r t} \quad \text{where} \quad \omega_r = \sqrt{\frac{k_{leg}}{I}} \\ \theta_b(t) &= \theta_b e^{i\omega_b t} \quad \text{where} \quad \omega_b = \sqrt{\frac{k_{bridge}}{I}} \end{aligned} \quad (3.11)$$

As a result of this analysis one can see that the device designs have rocking and bending modes that are governed independently by the stiffnesses of the legs and bridge, respectively.

3.1 Damping

The only forces considered in the above derivation of the theoretical response were those from the individual spring constants of the silicon legs and bridge. Another significant contribution to the overall device response is the viscous damping due to the device moving through the surrounding air. To add the effects of damping to the theory, Lagrange's equation of motion

((3.8)) must first be changed to include a velocity-dependent dissipative term, namely [26]

$$\frac{d}{dt} \left(\frac{\partial \mathcal{L}}{\partial \dot{\theta}_i} \right) = \frac{\partial \mathcal{L}}{\partial \theta_i} - \frac{\partial f}{\partial \dot{\theta}_i} \quad (3.12)$$

where f is the dissipative torque defined by $-\alpha \dot{\theta}$. The damping ratio, C is then defined by

$$C = \frac{\alpha}{2I}$$

and Equations (3.11) become

$$\begin{aligned} \theta_r(t) &= \Re\{\tilde{\theta}_r e^{i\omega'_r t} e^{-C_r t}\} \\ \theta_b(t) &= \Re\{\tilde{\theta}_b e^{i\omega'_b t} e^{-C_b t}\} \end{aligned} \quad (3.13)$$

The primes on ω'_r and ω'_b indicate that they are slightly perturbed from the undamped resonances, namely,

$$\omega'_r = \sqrt{\omega_r^2 - C_r^2}$$

and similar for ω'_b . Taking the real part of (3.13)

$$\begin{aligned} \theta_r(t) &= \theta_r e^{-C_r t} \cos(\omega'_r t + \phi_r) \\ \theta_b(t) &= \theta_b e^{-C_b t} \cos(\omega'_b t + \phi_b) \end{aligned} \quad (3.14)$$

which are both systems that oscillate at frequency, $\omega'_{(r \text{ or } b)}$, with a decaying amplitude governed by the value of C . If the oscillator is driven with a sinusoidal force, $\Gamma = p(\phi, P_0) s \cos \omega t$, where ω is the (arbitrary) frequency of the oscillating force, $p(\phi)$ is the net incident pressure amplitude, and s is the area of the device, the amplitude of oscillation increases exponentially towards a steady-state value given by[26]

$$\begin{aligned} \theta_r(\omega) &= \frac{P_0 \cdot s}{I \sqrt{(\omega_r^2 - \omega^2)^2 + \omega^2 C^2}} \\ \theta_b(\omega) &= \frac{P_0 \cdot s}{I \sqrt{(\omega_b^2 - \omega^2)^2 + \omega^2 C^2}} \end{aligned} \quad (3.15)$$

It is important to remember that the force on the wing is a function of the phase difference between the two wings as well as between the front and back of the device, which is, in turn,

affected by the angle of incidence.

The potential damping forces for beam shaped oscillators were studied in [27] and it was determined that the most significant effect is due to squeeze-film damping and the second most significant is due to air damping. For devices with trenched substrates, the squeeze-film damping is virtually eliminated, making the designed devices damped primarily by viscous air damping. Under that assumption, the finite element models implement damping using the formula given by [28]. In this case, the damping coefficient per unit area is given by

$$\pi \sqrt{b\rho\omega\mu}$$

where ρ is the density of air (1.21 kg/m³), ω is the angular frequency of incident sound, μ is the viscosity of air, and b is an empirical parameter determined in [28] to be approximately 2 for rectangular cantilevers. The damping ratio, C , is then given by

$$C = \frac{s \cdot \pi \sqrt{b\rho\omega\mu}}{2I} \quad (3.16)$$

3.2 Comb Fingers

The last requirement to produce a useable micro-scale device was to develop a viable readout scheme to determine oscillation amplitude. The primary method used in the laboratory to measure device performance was by Laser Doppler Vibrometry (LDV - to be explained in further detail in Chapter 5). Other approaches employed include optical gratings on the outer edge of each wing to be read out with a series of photosensors as described in [21] - a design that was later similarly employed by Miles, et al., in [9]. An alternative method proposed in [21] was to use an electrostatic readout using interdigitated comb-finger capacitors.

Many MEMS devices utilize capacitive readout techniques, and many use comb fingers. Generally, comb-finger devices attempt to minimize the mechanical noise of the device by electrostatically maintaining the position of the device and using that electronic control signal to readout the particular device response.[29] The devices developed in this research, however, require the device to achieve its full amplitude at resonance to induce the forces between the two wings so the phase difference ($\omega\tau$) and amplitude can be mechanically amplified to determine the direction of the incident sound. Such a design can be coupled with an external electronic circuit like that found in Irvine Sensors' MS3110 Capacitive Readout Integrated Circuit (IC), and ca-

capacitive fingers have been designed into all later devices for that purpose[30, 31]. Thus far, the comb fingers used in this research are $2\text{ }\mu\text{m}$ wide and $100\text{ }\mu\text{m}$ long with a $2\text{ }\mu\text{m}$ gap between alternating fingers as can be seen in Figure 3.4.

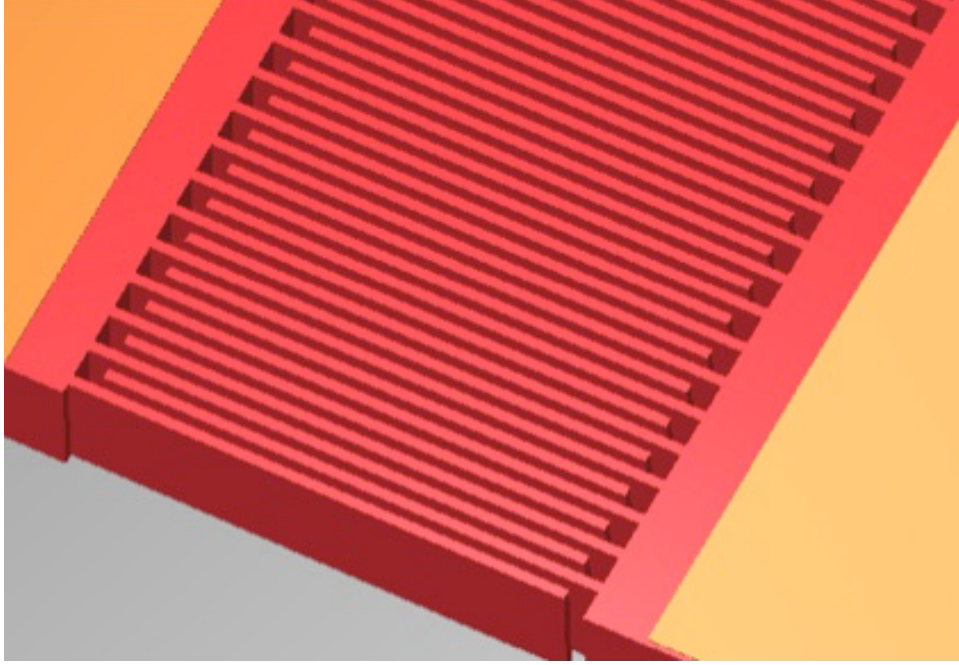


Figure 3.4: Comb finger design in L-Edit. Fingers are $2\text{ }\mu\text{m}$ wide, $100\text{ }\mu\text{m}$ long, and $10\text{ }\mu\text{m}$ thick.

As the wings of the device move vertically in and out of the substrate, the capacitance changes proportionally. In order to maximize the capacitance between the device fingers and substrate, the maximum surface area possible must be designed, which is accomplished by minimizing the width of the comb fingers and placing as many as possible along the perimeter of the device. According to the SOIMUMPS process design rules, the minimum SOI feature size is $2\text{ }\mu\text{m}$, which we have used as the finger width in all our designs.

The capacitance in a parallel-plate capacitor is given by

$$C = \frac{\epsilon_0 A}{d}$$

where ϵ_0 is the permittivity of free space ($8.85 \times 10^{-12}\text{ F/m}$), A is the surface area, and d is the distance between the plates. Placing this in the context of the capacitive comb fingers for

electronic readout,

$$A = l \cdot h \cdot n = 10^{-4} \cdot 10^{-5} \cdot n \quad [m^2]$$

where l is the finger length, h is the device layer height, and n is the number of comb finger capacitors or twice the number of comb fingers (generally 125 per side or 250 total). d is designed to be $2 \mu\text{m}$. This gives an overall capacitance for one side of the device of approximately (neglecting fringing and finger ends)

$$C = \frac{8.85 \times 10^{-12} \cdot 250 \times 10^{-9}}{2 \times 10^{-6}} [F] \approx 1 \text{pF}$$

Each device responds with a slightly different amplitude, but Figure 6.4 shows that an amplitude of one micron is a reasonable approximation within an order of magnitude for a typical device. In that case

$$\begin{aligned} C &= \frac{\epsilon_0 A}{d} = \frac{\epsilon_0 l(h-y)}{d} \\ \Delta C &= -\frac{\epsilon_0 l}{d} y \end{aligned} \quad (3.17)$$

where y is the displacement of the end of the wing from its equilibrium position. Setting y to $1 \mu\text{m}$, the corresponding change in capacitance is

$$\begin{aligned} |\Delta C| &= \frac{8.85 \times 10^{-12} (250 \cdot 10^{-4})}{2 \times 10^{-6}} 10^{-6} [F] \\ &= 1.1 \times 10^{-13} \text{ F or } 110 \text{ fF} \end{aligned}$$

Given that the MS3110 readout IC reports a sensitivity to $4 \text{ aF}/\sqrt{Hz}$ ($1 \text{ aF} = 10^{-18} \text{ F}$), this design of comb finger capacitors provides adequate capacitance to allow us to use this off-the-shelf solution.

3.3 Finite Element Modeling

Devices are initially designed using the Computer Aided Design (CAD) tool in the COMSOL MULTIPHYSICS software package to test the frequency response. The two dimensional footprint is first drawn and then extruded by $10 \mu\text{m}$ in the z-direction and material type is set to single-crystal silicon, Si(c). By matching experimental results with the FEM results, the appropriate Youngs' modulus and shear modulus for the silicon device layer used in the SOIMUMPS

fabrication process were determined to be 145 GPa and 35 GPa, respectively. This is important to ensure accurate modeling in the future due to the orthotropy of Si(c).

The net forces on the device are due to a sound-field that is complicated by both the device itself and the packaging around the device. In order to more accurately model the forces due to incident sound, a cylinder of air is added to the design model that completely envelopes the device, a process that was optimized in [32]. At the outer boundary of this air column is a Perfectly Matched Layer (PML) which is modeled such that any incident sound pressure is completely absorbed in the PML. This allows the device to be effectively treated as being completely in the far-field and not impacted by reflections from the model boundaries.

As reported in [31], these models used Equation (3.16) with the fitting parameter, b , of 12 to match the frequency bandwidths at the two resonance peaks. The value of b is larger than that typically used for rectangular cantilevers (≈ 2)[28] due to the additional damping associated with the comb fingers attached to the wings. The use of this larger value of b is justified since the addition of the combs increases the perimeter by about an order of magnitude. The combs also operate in close proximity to the surrounding device layer and substrate which likely induce some squeeze-film and slit resistance as studied in [33].

Prior to running the finite element model, the device and sound field are first converted to a mesh that is relatively coarse throughout the air column and wings of the device and finer near the legs to accurately reflect the narrower features there. The air column boundaries are then set to *Radiation Condition* to induce a sound field that can be adjusted to different incidence angles so a parametric sweep of angles can be conducted later to determine the directional dependence of the response. While most devices have comb fingers or perforated wings (or both), these features are not modeled in COMSOL because they increase the degrees of freedom to the point that the equations are unsolvable with the memory capacities of even most multi-core computers. A correction to the device density is manually added to compensate for the mass removed in the perforations and between the comb fingers. The damping coefficient is manually adjusted depending on the device dimensions and number of comb fingers, which will be further described in Section 6.4.

Once the model is completed, the solver is used to find the eigenvalues of the system. Then a parametric sweep of frequencies is conducted across a frequency range that includes the eigenvalues representing the rocking and bending modes. Figure 3.5 shows the output of the frequency sweep for a device similar to the one shown earlier in Figure 3.2. The frequency

response closely matches that from the simpler mechanical model shown in Figure 2.7, which was developed using the reported spring and damping constants determined by Miles, et al[6]. This implies that the FEM dimensions yield a device whose response is closely matched to that of the actual fly.

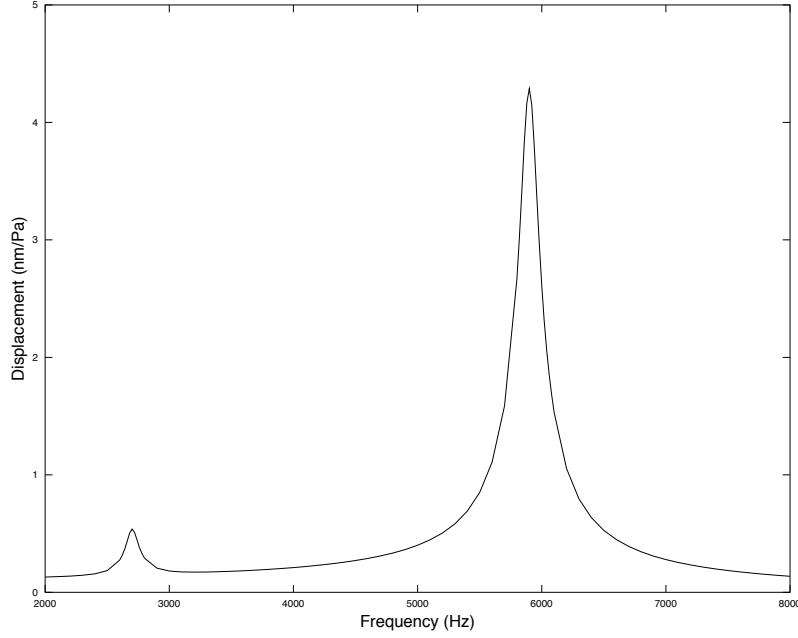


Figure 3.5: Frequency response of a finite element model based on the *Ormiine* hearing system.

3.4 Pressure Gradients

One difficulty with the early iterations of devices was that the response amplitude was too small to be practically readable. It was theorized [21] that this was due to squeeze-film damping, so all devices designed since were fabricated using SOIMUMPS because it allows the user to remove the bottom substrate using Deep Reactive Ion Etching (DRIE), as in Figure 3.6. When mounted on an open-backed package, this allows free-communication between the backside of the device and the ambient sound field.

Because the substrate beneath the device has been etched to eliminate squeeze-film damping, incident sound is able to diffract around the SOI surrounding the device as well as the packaging and impact the backside of the device. The phase difference induced by the travel time around the device and packaging causes a net pressure difference that forces the wings into motion.

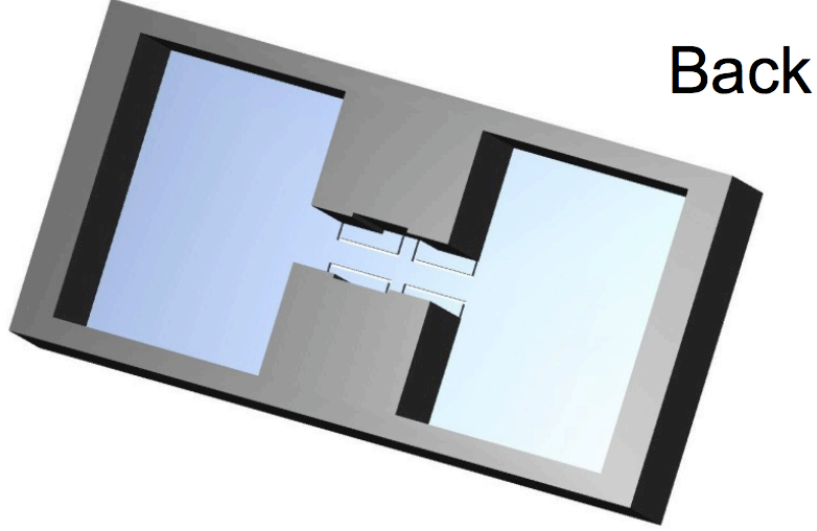


Figure 3.6: Designed structure (bottom side).

The net acoustic pressure is given by [34]

$$P_{net} = P_0(1 - e^{ikL \cos \theta}) \quad (3.18)$$

where P_0 is the unperturbed sound pressure amplitude at the device location, k is the wavenumber, L is the path length difference between the top and bottom of the device, which depends on the geometry of the SOI and packaging surrounding the device. This is a typical response among the class of acoustic receivers known as *pressure gradient* microphones. The resultant effective pressure is the difference of the individual pressures on the two faces. While the transient pressure profile on each face is similar, the difference in pressures occurs because the diffracted sound lags the directly-incident sound by the amount of time it takes the sound to travel to the rear face of the device. If the device is a thin ribbon or plate and sound is incident from the side, the incident pressure on both the front and back face of the plate are in-phase because the two are equidistant from the source. Conversely, if the sound is incident normally on one face, the path-length difference between the two faces is maximal as the sound must travel all the way around the edge of the device. If 0° is defined by normally-incident sound, the pressure-gradient receiver will demonstrate a *cosine* dependence on incidence angle.

The effect of the pressure gradient induced by the packaging is that the effective incident pressure varies from zero to twice the actual incident pressure depending on the wavelength and L . In Figure 3.7, the directional dependence of the net sound pressure on a theoretical pressure-

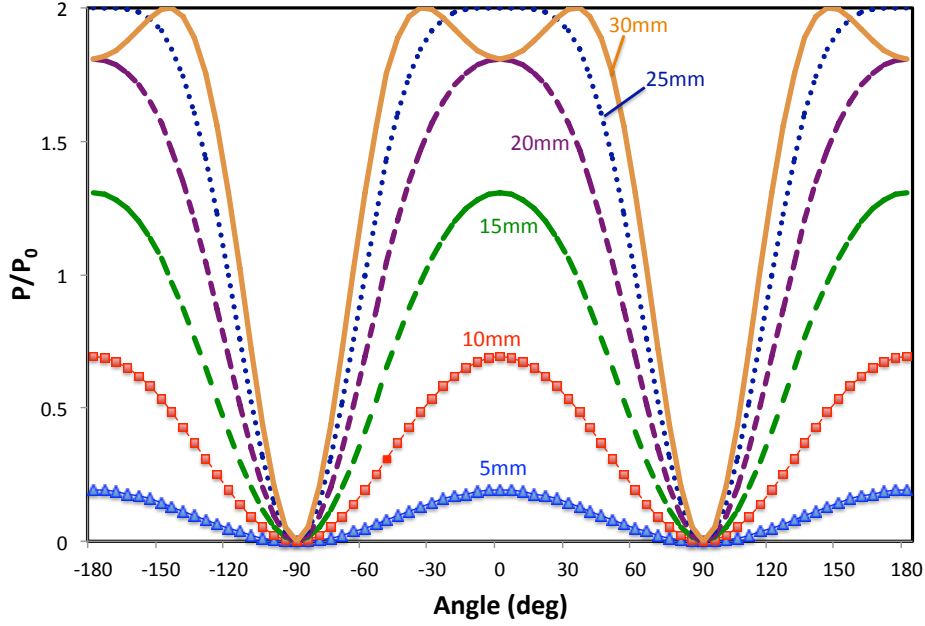


Figure 3.7: Relative angular response of a pressure gradient microphone for several aperture sizes versus a wavelength of 5 cm.

gradient microphone is shown for several values of L , assuming a wavelength of 5 cm. As seen in the figure, in this configuration a microphone that is much smaller than the wavelength of sound still has a much reduced amplitude because the sound diffracted around the device is nearly in-phase on both sides and greatly reduces the net force on the device. Also, if the packaging dimensions are such that $L \geq \lambda/2$, the number of lobes increases and the directional response becomes much more complicated, to the point where the device would be unusable for actually determining the direction.

Incorporating the pressure gradient into the design by etching the substrate beneath the device allows for some additional flexibility with the design. Because the rocking mode amplitude is much smaller than that of the bending mode, it may be too small to be practically useful. In this case, the latter can be combined with an omnidirectional microphone and the device response can be calibrated to the incident sound pressure level, allowing the user to determine direction.

Once the FEM was optimized to model devices as being forced acoustically instead of through direct contact, the packaging could be inserted into the model to explore the full impact of the pressure gradient. This was presented in [32] and consolidated results from that work are seen

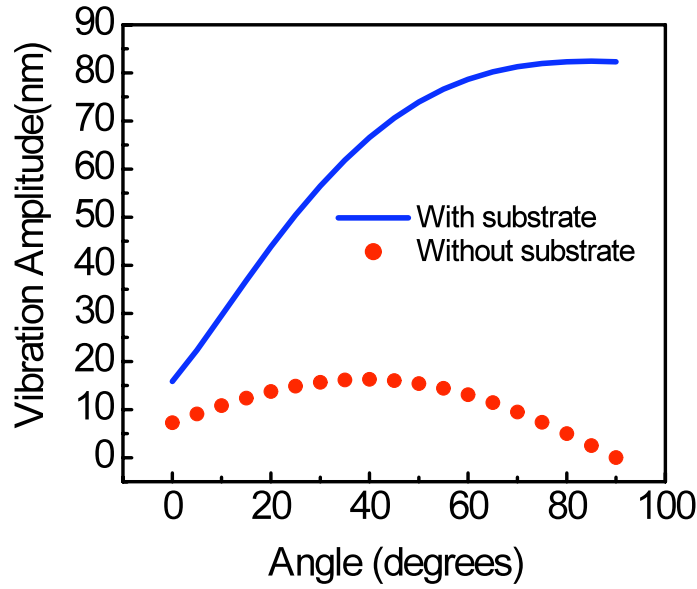


Figure 3.8: FEM (COMSOL) rocking-mode response to a device with and without a surrounding substrate.[32]

in Figure 3.8. When the device is surrounded by a baffle, the response approaches the original theoretical response as the baffle approaches infinite area. The impact of closing the substrate beneath the device was also studied [25] and it has the same effect as adding an infinite baffle because it eliminates the sound pressure variations on the back side of the devices, making them respond according to the initial mechanical theory with a directionally independent bending mode and a rocking mode that increases as the sine of the angle.

3.5 Chip Layout

Because each SOIMUMPS design is fabricated on a $1\text{ cm} \times 1\text{ cm}$ die area, several devices can be included on a single fabrication run. Each design iteration has, therefore, included between four and twelve devices with some variation among them to test the mechanical or electronic impact of individual design features. One typical design was shown in Figure 3.4, and dimensions of the device are presented in Table 3.1.

Once the model is tested in COMSOL, it is transferred (manually redrawn) into MEMS-Pro/L-Edit Software, including any perforations and comb-fingers. Each device is created individually in L-Edit, then several designs are arranged onto a single chip for fabrication. Due to design-rule

limitations for the SOIMUMPS process, the SOI layer is filled into the area between individual devices leaving just enough separation for electrical isolation, with a line of SOI running to the outside edge of the device for easier signal output. A layer of gold is also deposited onto this trace to minimize resistivity and allow wirebonding after fabrication. Figure 4.9 shows an SEM image of a fabricated chip with several gold traces leading to the edge of the device.

Table 3.1: Dimensions of fabricated device shown in Figure 4.7.

Component	Dimensions (μm)
Wing	1000×875
Bridge	400×500
Leg	100×50
Finger	2×100
Gap between fingers	2

In order to completely isolate individual devices so they can be mounted on smaller packages and the impact of the surrounding substrate size studied, a $200 \mu m$ subdicing trench can be etched through the chip. The entire chip is then held together with narrow ($10 \mu m$) SOI bridges across the trench, placed every $100 \mu m$, which are easily broken by simply pressing the center of the chip from the backside. A computer drawing of a trenched design can be seen in Figure 3.9.

The purpose of this chapter was to present the general structure of the designed devices as a whole. A number of the design features have been studied by varying the general design and those individual topics will be discussed in the remaining chapters. The exact specifications of individual device designs are presented in the Appendix, and the results of the fabrication are shown in Chapter 4.

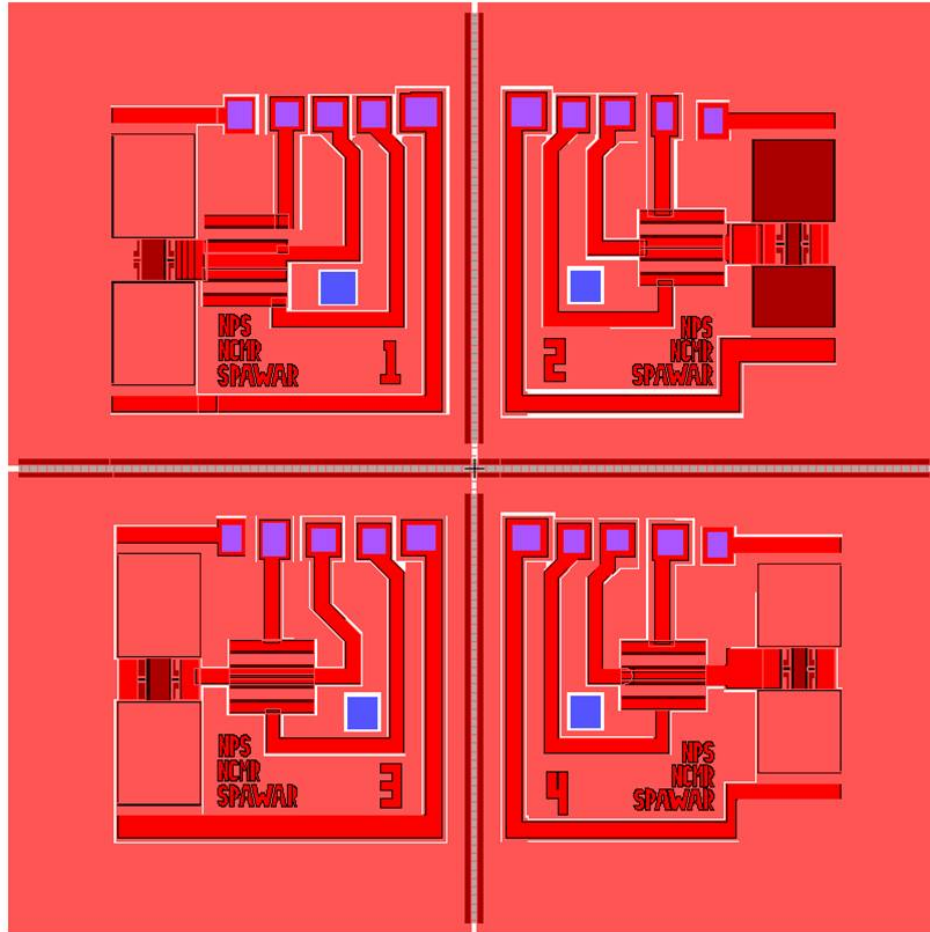


Figure 3.9: CAD diagram of a four-device chip designed with 200 μm trenches running horizontally and vertically through the chip to allow easy separation of individual devices.

THIS PAGE INTENTIONALLY LEFT BLANK

CHAPTER 4:

Fabrication

This chapter outlines the fabrication steps used to create the devices once the design is submitted. As stated in the last chapter, the process is performed by MEMSCAP, Inc. and details can be found in [35]. The MEMSPro / L-Edit software used to create the design files for fabrication allow the user to generate 3D images of the device during various stages of the micromachining process. The images presented throughout this chapter (with grateful appreciation to Jeffrey Catterlin for providing the images) show one-half of the device so the substrate can also be seen in various stages.

The fabrication process begins with a 400 μm thick silicon on insulator (SOI) substrate (Figure 4.1 with 1 μm thick SiO_2 and 10 μm thick device layers.

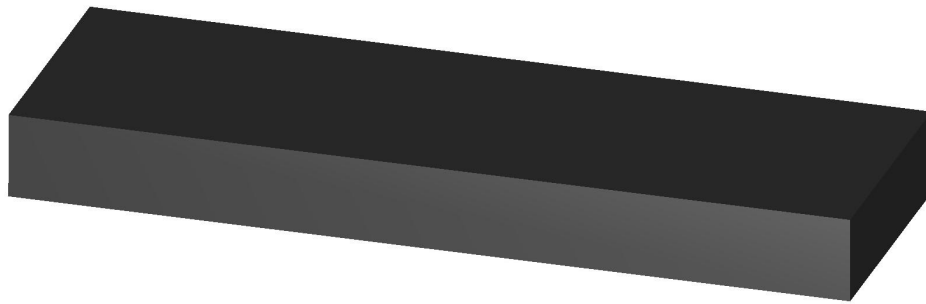


Figure 4.1: Substrate

Prior to micromachining, the device layer must be doped. This is accomplished by depositing phosphosilicate glass (PSG) on top of the device layer and annealing it in argon for one hour at 1050 °C. This forces phosphorus into the layer and the PSG is then removed using a standard wet etching process leaving only *n*-type, conducting silicon.

The next step is to deposit the first layer of metal for making interconnects and bond pads. A layer of negative photoresist is placed on the wafer, then it is illuminated through a mask to

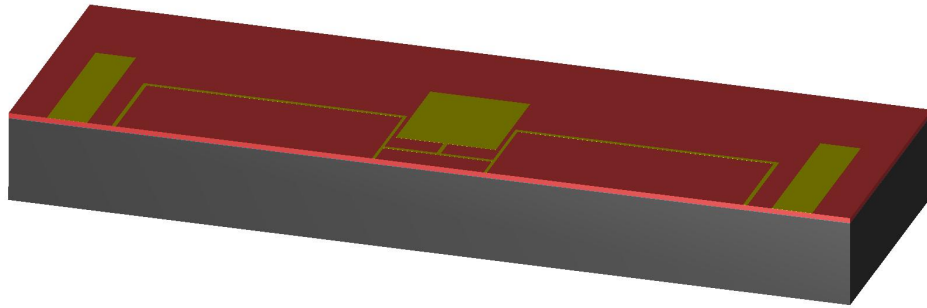


Figure 4.2: Deposition of pad metal onto substrate.

harden areas that will not be deposited with metal. The unexposed portions of photoresist are removed, and 20 nm of chrome is deposited on the entire wafer by electron-beam evaporation, followed by 500 nm of gold. Finally, the rest of the photoresist and its metal coating is removed from the hardened areas, leaving metal in only the desired places (Figure 4.2). Because this layer of metal is subjected to high temperatures later in the process it is generally used for coarse features ($> 3 \mu m$) that do not require an optically smooth finish.

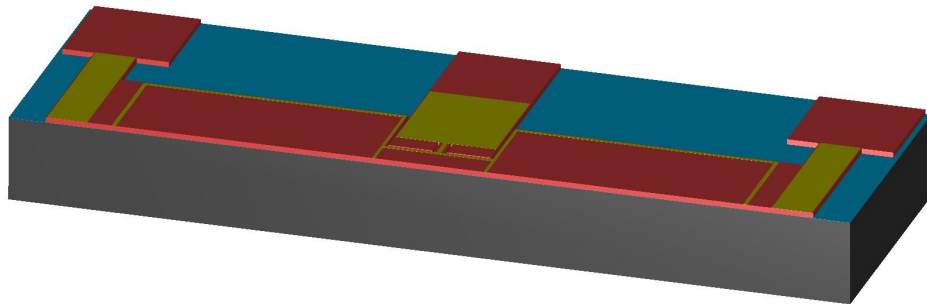


Figure 4.3: Etching Si device layer to form the mechanical structure.

Next, the wafer is coated with positive photoresist and exposed to ultraviolet light for defining

areas where silicon is to remain in place. Exposed areas of resist are softened and removed during developing. Then the device layer is Deep Reactive Ion Etched (DRIE) through the silicon to the oxide layer using an Inductively Coupled Plasma (ICP) leaving only the etched device as in Figure 4.3. It is important to note that the removal of the device layer is limited to 33% of the total area[35].

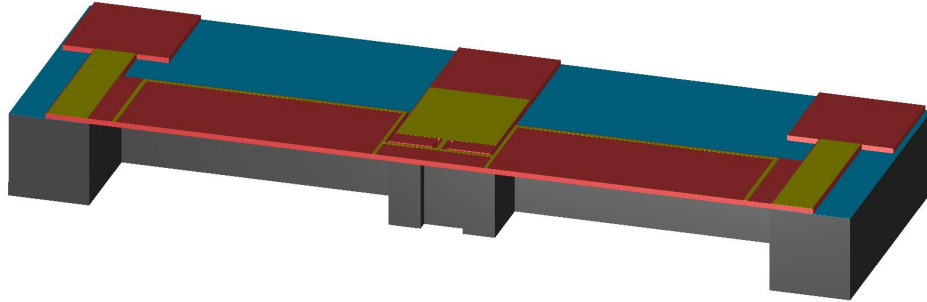


Figure 4.4: Substrate trenching by DRIE.

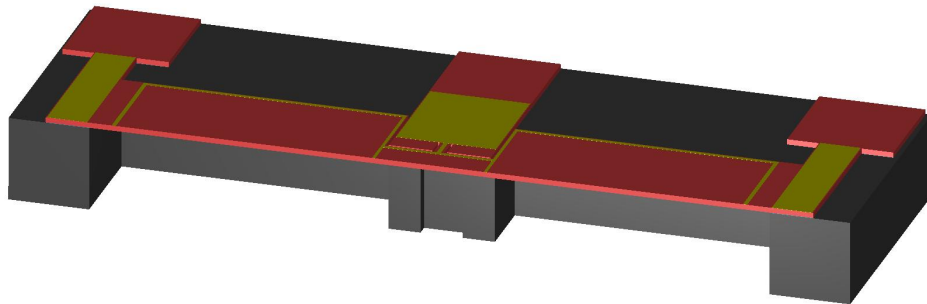


Figure 4.5: Oxide layer release by HF.

The bottom side of the substrate layer is initially covered with a protective oxide layer. This layer is Reactive Ion Etched (RIE) after being lithographically patterned with photoresist as

described above, and the substrate is subsequently etched using DRIE (Figure 4.4). The area of the trench should not exceed 20% of the total area[35]. Throughout this step, the topside of the device is coated with a protective layer so it is not damaged during wet-etching of the oxide layer (Figure 4.5) through the trenched substrate to release the mechanical structure. Once this is complete, the protective layer is dry-etched off the top and the device layer is released as designed. Finally, blanket metal (50 nm Cr + 600 nm Au) is deposited using electron beam evaporation through the final mask (4.6) onto either the device layer or exposed areas on the top side of the substrate layer.

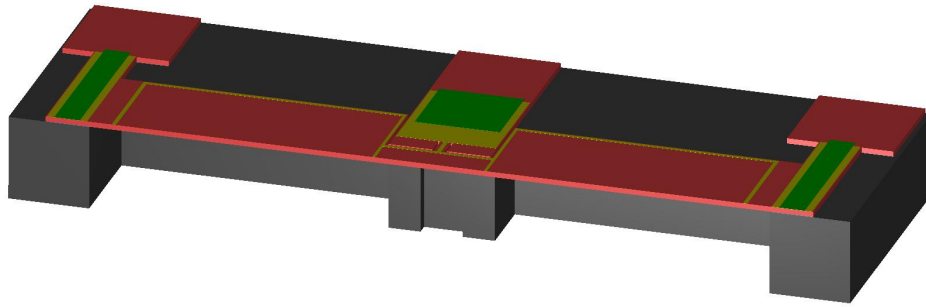


Figure 4.6: Blanket metal deposition

4.1 Fabrication Results

Once fabrication is complete, the wafers are diced and fifteen dies of each design submitted are sent to the respective designers. One device after fabrication is shown in Figure 4.7.

Figure 4.8 shows an SEM image of the device comb fingers after fabrication. It should be noted that the capacitors appear fully engaged at rest and very little curling is seen due to residual stress after the device layer was released.

Figure 4.9 shows an SEM image of a fabricated chip with several gold traces leading to the edge of the device, and Figure 4.10 shows an entire chip that included subdicing trenches.

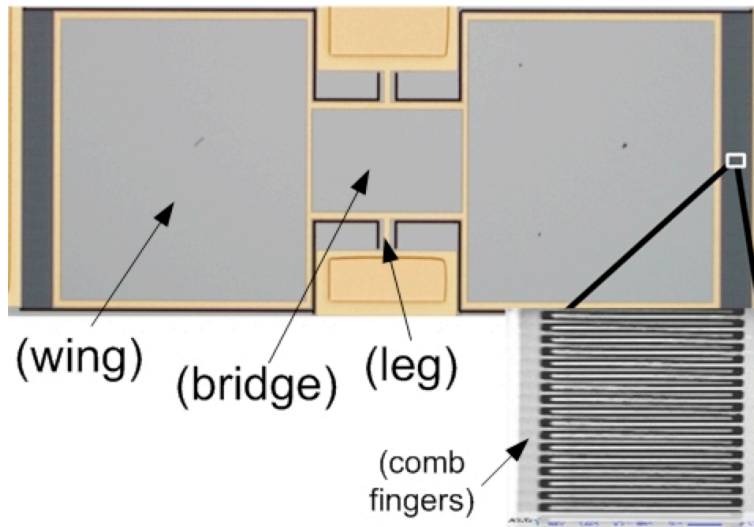


Figure 4.7: Photograph of device (also published in [31]). Inset is further magnified view of several capacitive comb fingers.

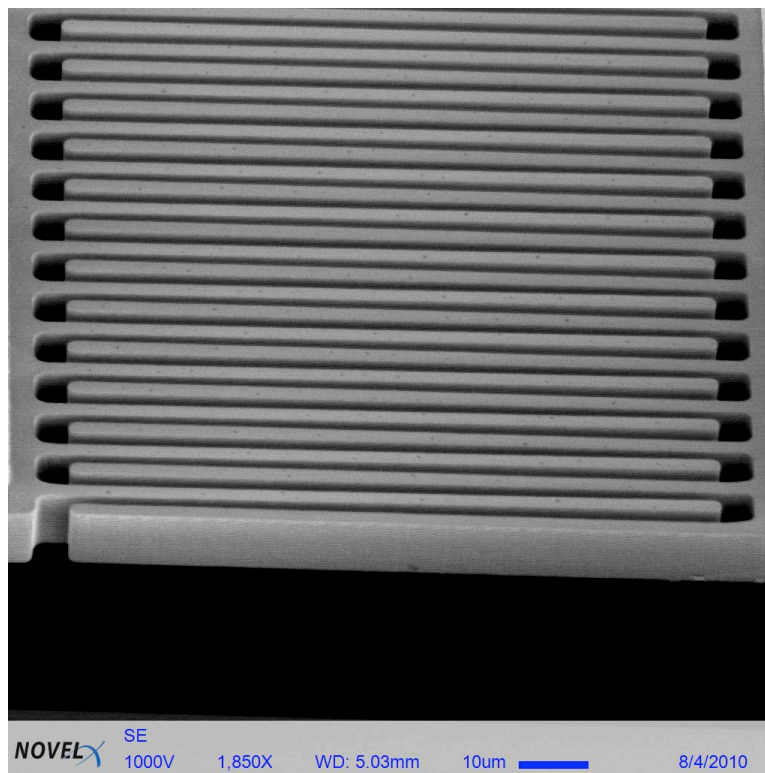


Figure 4.8: SEM image of comb fingers, image magnified 1850x. Thanks to Abby Hoffman of Stevenson School for her work obtaining this image.

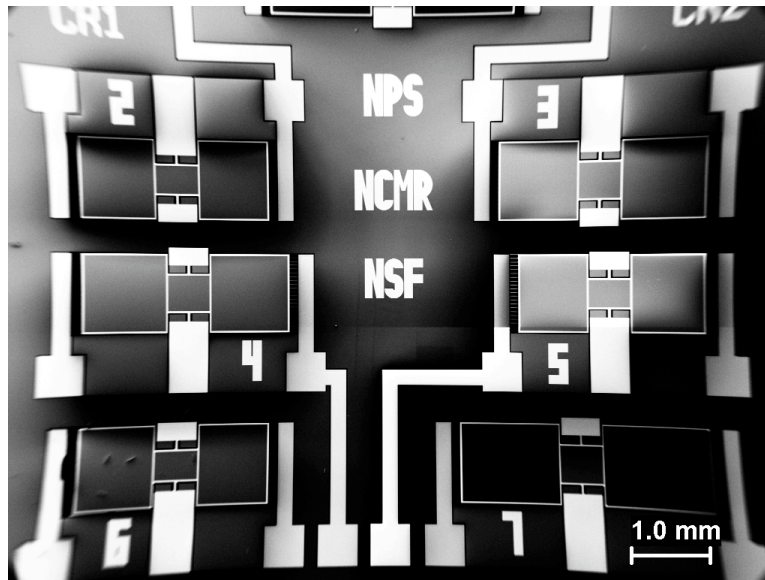


Figure 4.9: SEM image of a portion of one of the chips fabricated during the reported research. Bright squares and connecting lines are gold traces for electronic signal routing and wirebonding.

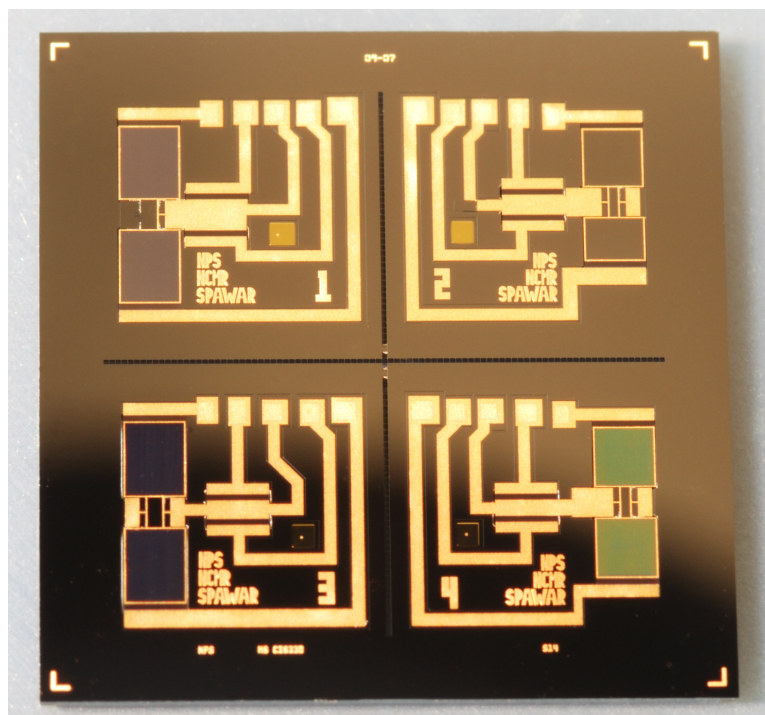


Figure 4.10: Photo of chip shown in Figure3.9.

CHAPTER 5:

Measurement Setup

Once devices are received from the foundry, the individual die are lifted from their shipping tape and mounted in one of a number of different package types. The first die tested is generally mounted by conductive silver paste onto a plastic pin grid array (PGA) socket (Mill Max part no. 515-13-124-13-041001, for example) as seen in Figure 5.1. These are manufactured with a square opening through the center that is large enough so that the back side of every device on the chip is unobstructed by epoxy and by the plastic socket frame. The device pads are then wirebonded to the top of individual socket pins using a K&S 4525AD wirebonder so the same device can be used for mechanical and electrical testing. Wirebonder settings are as listed in the Appendix of [36].

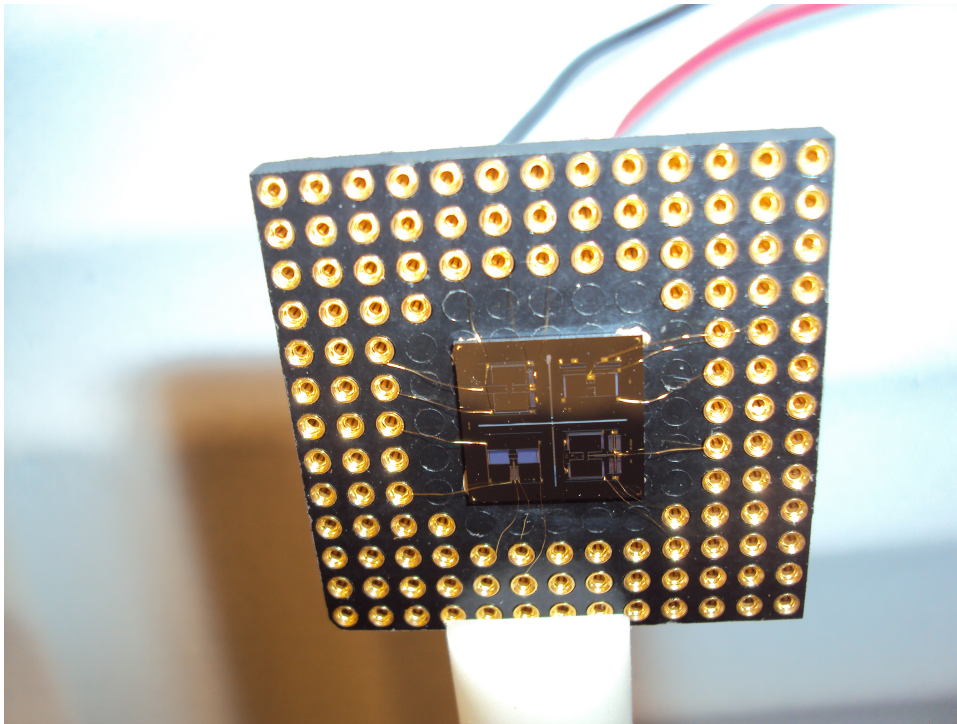


Figure 5.1: Device mounted on plastic PGA and wirebonded to various pins.

Another packaging method used for testing is to mount the individual device on the edge of a Plastic Small Outline IC (PSOIC) package as seen in Figure 5.2. The advantage of this package is that the cavity is just wide enough to hold a single device once it is separated using

the subdicing trenches. The package can be easily cut so the backside of the device is still unobstructed, and it has bond pads instead of the socket rims that are used when bonding to PGA sockets. This makes a much more compact package with bonds that are more secure, but have much smaller pins making it much more difficult to use removeable external connections. The existing electronic readout chip uses the same package type, so a custom circuit board can be used for either the MS3110 readout chip (explained in Section 5.2), or an SOIC containing an MS3110 die bonded directly to the device to minimize capacitance and noise effects as long as the pinout matches the prepackaged IC.

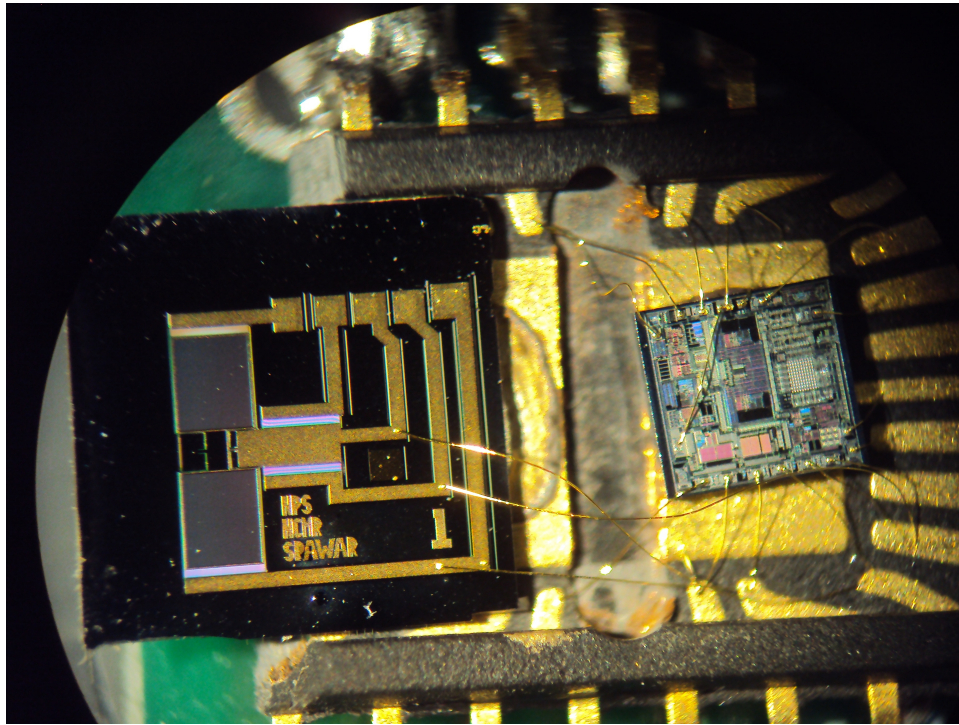


Figure 5.2: Microscope image of device mounted on plastic SOIC and wirebonded to MS3110 die.

In general, the device under test is mounted atop a metal or phenolic post which is attached to a moveable stage on a standard vibration-isolating optics table. An arm is mounted with its rotation axis directly above the mounting post and holds a Selenium DH200E compression driver (speaker) which provides the sound source for all measurements as shown in Figure 5.3. The speaker is driven (through a power amplifier) by either a function generator or computer, depending upon the particular experiment.

The outlet of the driving speaker measures one inch (25 mm) in diameter, and the lowest fre-

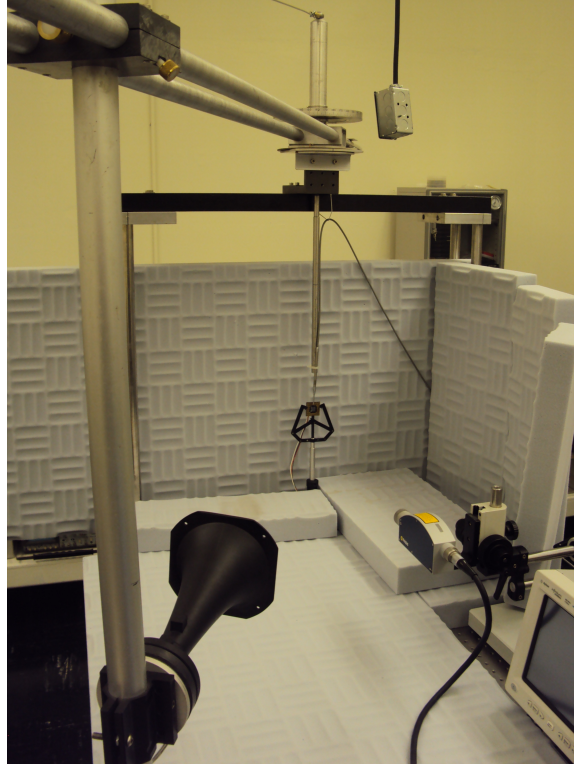


Figure 5.3: Laboratory setup showing rotating speaker arm and device mounting.

quency of interest during the course of this research project is approximately 1400 Hz, so the longest wavelength is $\lambda = c/f = 343/1400 = .245m$. This, in turn, yields a parameter ka of $2\pi a/\lambda = 0.32$, where a is the radius of the speaker outlet and k is the wavenumber. Assuming the driver is equivalent to a simple circular piston of radius 13 mm, the transmitted beam pattern should be a single lobe, which is verified using a reference microphone as can be seen in Figure 5.4. Also the speaker is mounted such that the distance from the device (r) places it in the far-field ($r \gg a$). Given the small size of the device and the relatively long distance from the speaker, the incident sound can be approximated as a plane wave.

5.1 Laser Vibrometry

The most accurate measurements of the mechanical response of the devices are obtained using optical means and this is done to characterize each newly designed and fabricated device. The laser from a Polytec OFV-534 laser doppler vibrometer (Figure 5.5) is focused on the outer ends of the device so that the beam is reflected directly back into the laser head and the device is driven with an acoustic signal. The laser head is connected to an OFV-5000 controller, VDD-Z-

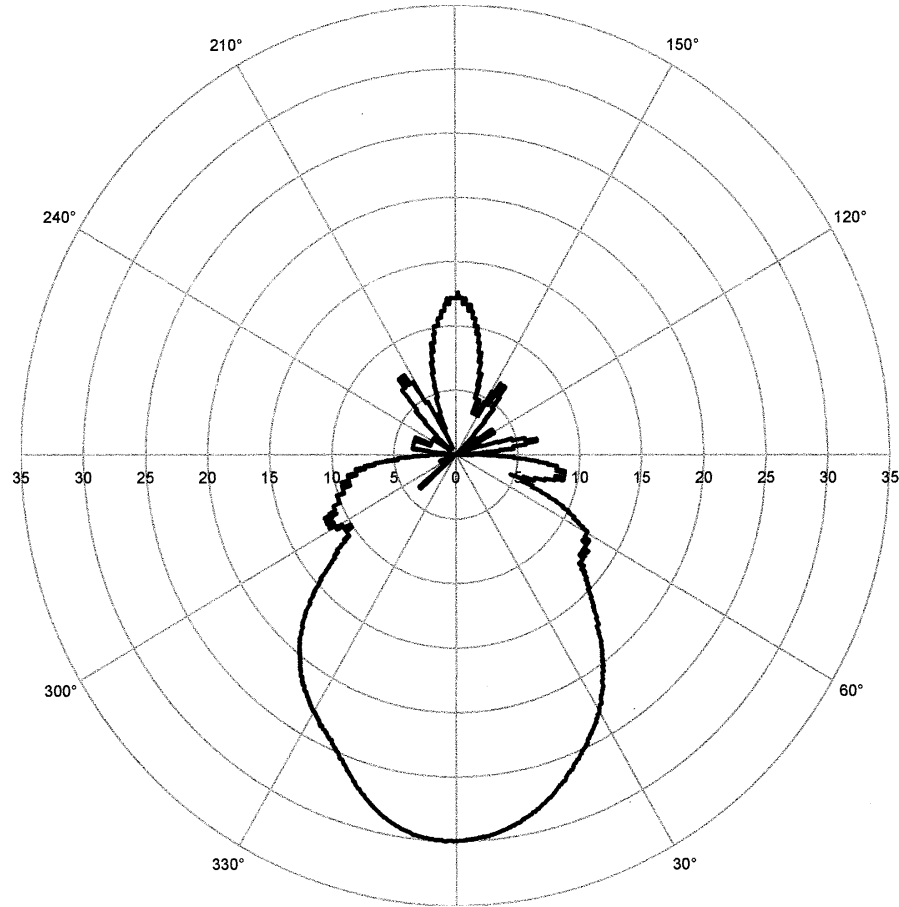


Figure 5.4: Directivity pattern of the speaker used for device testing.

011 junction box, and to a desktop computer through a National Instruments PCI-6110 interface.

The laser vibrometer is primarily composed of a Michelson interferometer in which one half of a split laser beam is used as a pathlength reference versus the other half of the beam which senses the motion of the surface reflecting the beam. Both beams are recombined and enter a detector that allows the system to output the velocity of the vibrating surface, given by the modulation frequency of the interference fringes. The reference beam also passes through a Bragg cell that shifts the frequency by 40 MHz, introducing a modulation of the recombined beam and allowing the detector to differentiate the direction of the motion (whether towards or away from the beam source). The laser in the Polytec system used during the course of this research is a helium neon laser ($\lambda = 633 \text{ nm}$).

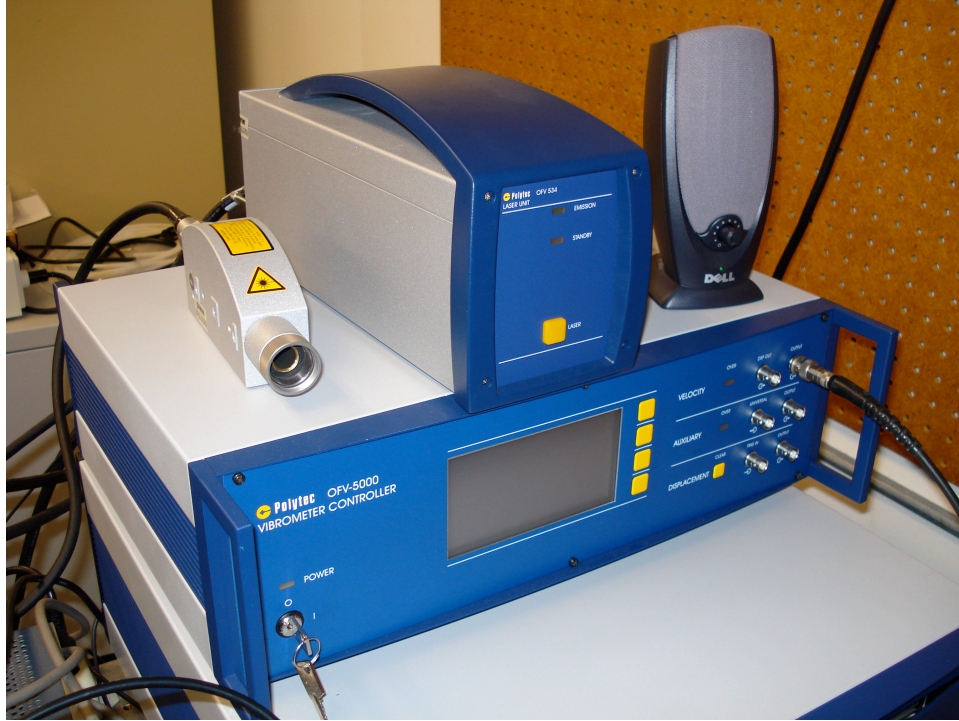


Figure 5.5: Polytec Laser Vibrometer system used for device measurement.

VibSoft software (Version 4.7) is used to generate the desired driving signal and trigger the laser signal acquisition. To test the frequency response of the device, a frequency chirp is used along with appropriate software band-pass-filter settings. A reference (omnidirectional) microphone is mounted directly above the device (see Figure 5.3) to compare the resultant amplitude to the received sound pressure level. It has been seen experimentally that, due to the small size of the reference microphone, the presence of the microphone itself does not affect the device response.

When using the VibSoft software to obtain a frequency response curve, the sample time, frequency resolution, and bandwidth are all dependent on each other. The user selects the frequency range to be swept, and the number of lines used in the Fast Fourier Transform (FFT). Increasing the number of FFT lines improves the frequency resolution, but increases the required sample time, as expected. Typical sample times during this research are in the hundreds of milliseconds, and typical frequency resolutions are between one and five Hertz.

Though the device responds instantly to incident sound, at resonance it takes anywhere from three to ten milliseconds to achieve its full amplitude for the given incident sound pressure. This means that the amplitudes obtained using a frequency chirp are much smaller than those

achieved in the steady state. For this reason, once the frequency spectrum is known, the device is driven by a sine wave at the resonant frequency. The directional response of the device is then determined by finding the maximum (steady-state) response of the device for various angles, using the reference microphone to ensure the received sound pressure level is constant across all angles.

The reference microphone used throughout the research is a Bruel & Kjaer Type 4138, 1/8 Pressure-field microphone with a sensitivity of -60.5 dB re 1V/Pa (or 0.939 mV/Pa) with a Type 267070 Preamplifier. The power supply for the microphone also provides 60 dB gain. To convert the input signal at the reference microphone from voltage to sound pressure, the VibSoft software uses a manually inserted conversion factor (1.045 Pa/V).

5.2 Readout

The capacitive readout IC mentioned in Chapter 3, is an off-the-shelf solution for electrostatic readout of the device response and the schematic is seen Figure 5.6. The circuit is essentially a capacitive bridge that combines the device comb fingers with onboard trimming capacitors to complete and balance the bridge. The device (variable) capacitor, C_{dev} (not shown), connects the CSCOM and CS1 terminals while the fabricated reference capacitor, C_{ref} , completes the bridge by connecting CSCOM and CS2. The trim capacitors are adjusted so that

$$C_{dev} + CS1 \approx C_{ref} + CS2 \quad (5.1)$$

and the details of the operation of the MS3110 can be found in [37]. A combined functional diagram of the device and MS3110 is given in Figure 5.7.

The MS3110 alternates the voltage on the CS1IN and CS2IN terminals between 2.25V and ground so that the bias direction of the bridge alternates at approximately 100 kHz. This bias switching period must be much shorter than the time constant of the device so that the electrostatic force on the sensor due to the biasing voltage averages to zero over a single cycle of device oscillation due to sound[38]. The feedback capacitor, CF TRIM, allows the user to control the amplifier gain and the output is fed through a Sample and Hold circuit and into a low pass filter with cutoff frequencies selectable up to a maximum of 8 kHz. The output is buffered with a user-selectable final gain and output trim. The MS3110 also contains a digital section which provides the off-chip communication capability so the user can select the various settings for trimming capacitors, amplifier gain, and other calibration registers.

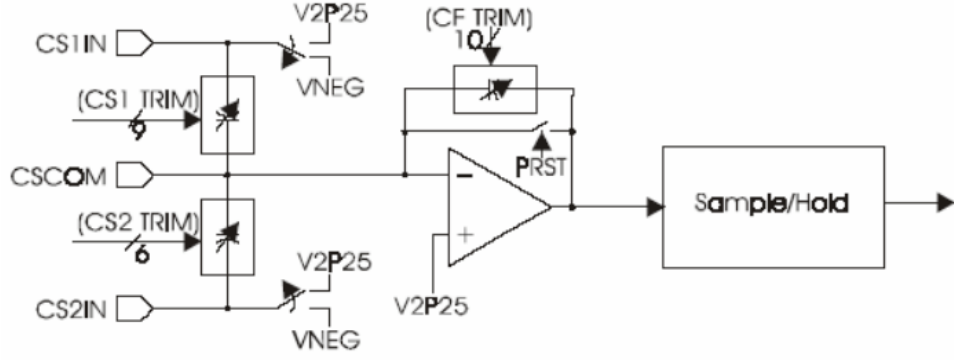


Figure 5.6: Simplified diagram of the electronic readout circuit within the Irvine Sensors MS3110 Capacitive Readout IC. From [37].

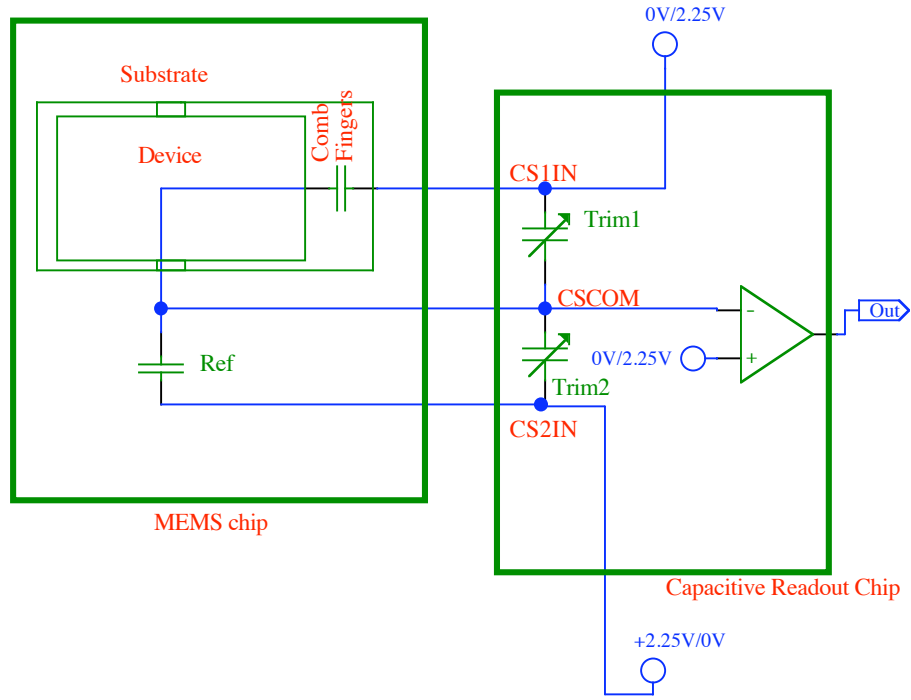


Figure 5.7: Circuit diagram of designed device capacitors and MS3110 readout chip.

The final output voltage is given by [37]

$$V_{out} = \text{Gain} \cdot V2P25 \cdot 1.14 \cdot \left| \frac{CS1_{tot} - CS2_{tot}}{C_F} \right| + V_{ref} \quad (5.2)$$

where $Gain$ is set to 2 or 4, $V2P25$ is the adjustable onboard voltage reference (nominally 2.25V), C_F is the selectable feedback capacitance, and V_{ref} can be set to either 2.25V or 0.5V by the user. $CS1_{tot}$ refers to the left side of Equation (5.1), and $CS2_{tot}$ refers to the right side.

The entire MS3110 circuit is contained in a small-outline integrated circuit (SOIC) package and when used with the associated development board, is placed into the designated socket and can be easily swapped with another IC. The development board contains power supply connections, pin headers to connect the device and reference capacitors, test points for all of the analog and digital signals, and a parallel port so the register settings can be computer controlled with the provided software. Register settings can also be burned into the chip's EEPROM memory with the software and an additional 16V power supply.

Once the device output pins are connected to the appropriate terminals on the development board, the chip is reset (by software via the parallel cable) and initial register settings are written into the memory. Generally the process begins by setting the feedback capacitance to approximately 10 pF, then both balancing capacitors are set to zero. Raising the value of $CS1$ to its maximum value should bring the signal (viewed on an oscilloscope) from 0 to 5 V or vice versa. If this does not happen, it is an indication that the maximum internal capacitance is less than that required to balance the entire bridge and the leads should be switched between the device and reference capacitors (or $CS1$ and $CS2$ terminals). The $CS1$ values are then adjusted until the output signal is approximately 2.25V. Reviewing Equation (5.2), one can see that reducing the feedback capacitance will increase the amplitude of the output signal. Setting the feedback capacitance too low may cause distortion or clipping for high amplitude signals; 1 pF is generally a reasonable compromise between signal strength and distortion. A screen capture from the oscilloscope monitoring the output of the balanced readout system under monochromatic sound excitation is shown in Figure 5.8.

5.3 Lock-in Amplifier

The MS3110 uses a four component bridge and drives the outer nodes of the balanced bridge so that the common node (CSCOM) potential is maintained as a virtual ground, halfway between the high and low voltages. As the device capacitance oscillates at the resonant frequency, the common-node voltage alternates above and below the virtual ground and this signal is measured as the output.

This process can be effectively reversed by driving the common node between the device and

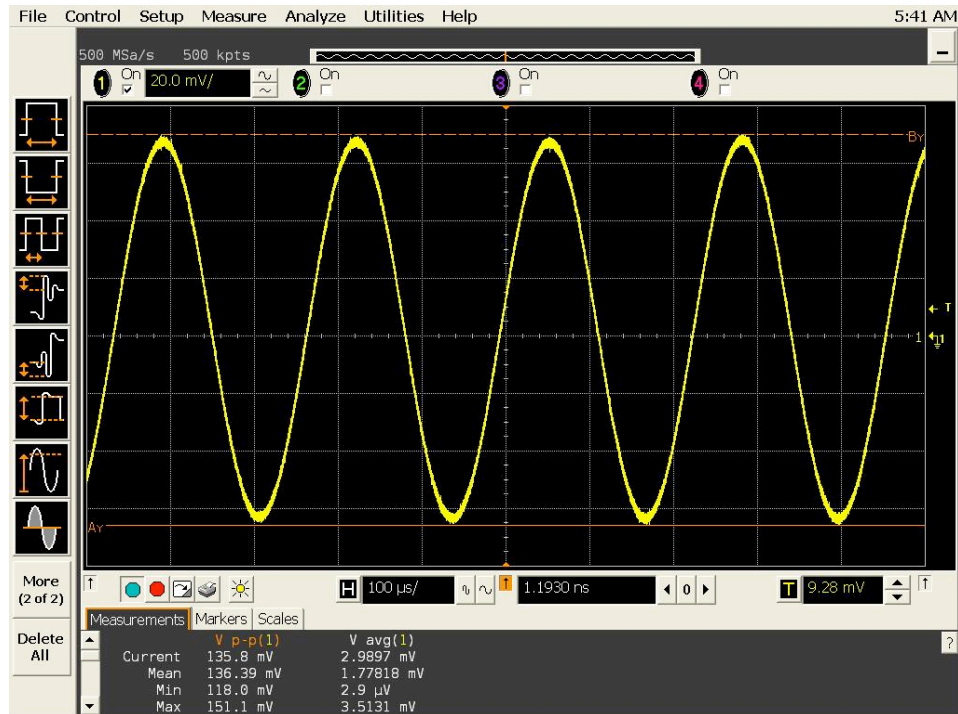


Figure 5.8: Electronic readout results for a device driven at its bending mode frequency (4348 Hz). Signal amplitude is approximately 138 mV_{pp}.

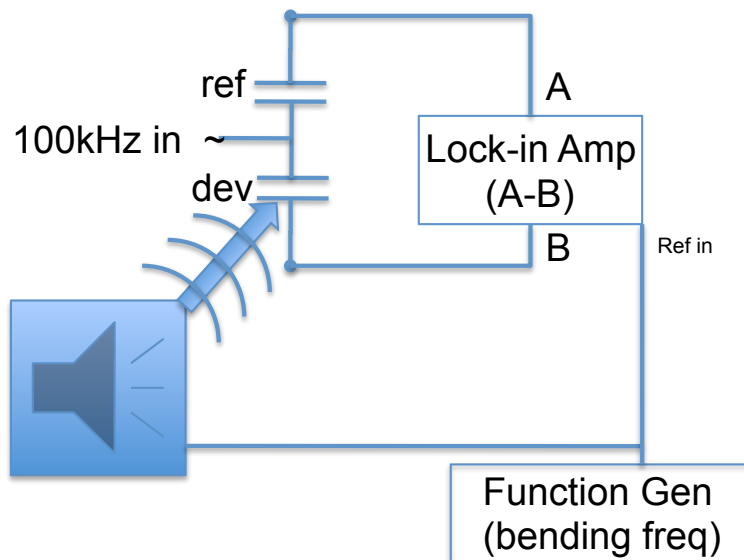


Figure 5.9: Block diagram for setup of lock-in amplifier for phase-sensitive detection of individual frequency components of device response.

reference (see Figure 5.9 with a high-frequency square wave similar to that used in the MS3110. By sampling the difference of the signals at the outer nodes (opposite sides of the common) of the two capacitors, the signal due to sound is riding on a carrier wave (the square-wave biasing signal). The high frequency can then be filtered to see only the amplitude of the device response.

Because the device response gives capacitance changes of femtofarads, the signal is almost entirely masked by the high-frequency carrier. One solution is to use a lock-in amplifier (LIA) referenced to a signal at the sound frequency (ω_s). If the reference signal fed into the LIA is given by

$$V_L = A_L \sin(\omega_s t)$$

and the difference signal from the two nodes (after filtering the high bias frequency) is given by

$$V_{dev} = A_d \sin(\omega_s t + \phi)$$

where ϕ is the phase difference between the reference and the remaining device signals, then ϕ is a constant as long as the two are actually phase-locked. The product of the two signals is then

$$V_f = V_L V_{dev} = \frac{A_L A_d}{2} [\cos \phi - \cos(2\omega_s + \phi)] \quad (5.3)$$

The AC portion of the combined signal is then filtered out leaving a DC signal proportional to the device response at the given frequency. This has been successfully accomplished using a 2.25 V_{pp}, 100 kHz square wave as the driving bias signal at the common node and a function generator driving a speaker and the lock-in reference at the bending-mode frequency.

CHAPTER 6:

Results

6.1 Frequency Response

The primary indicator that a device is working as designed is by analyzing its frequency response. It is a good validator of the model since it shows that the mass, spring constants, and damping ratios are as designed if the experimental frequency response matches well with that of the model. In Figure 6.1, the experimental frequency response is overlayed with the COMSOL modeling results for one of the sensors which clearly are very closely matched.

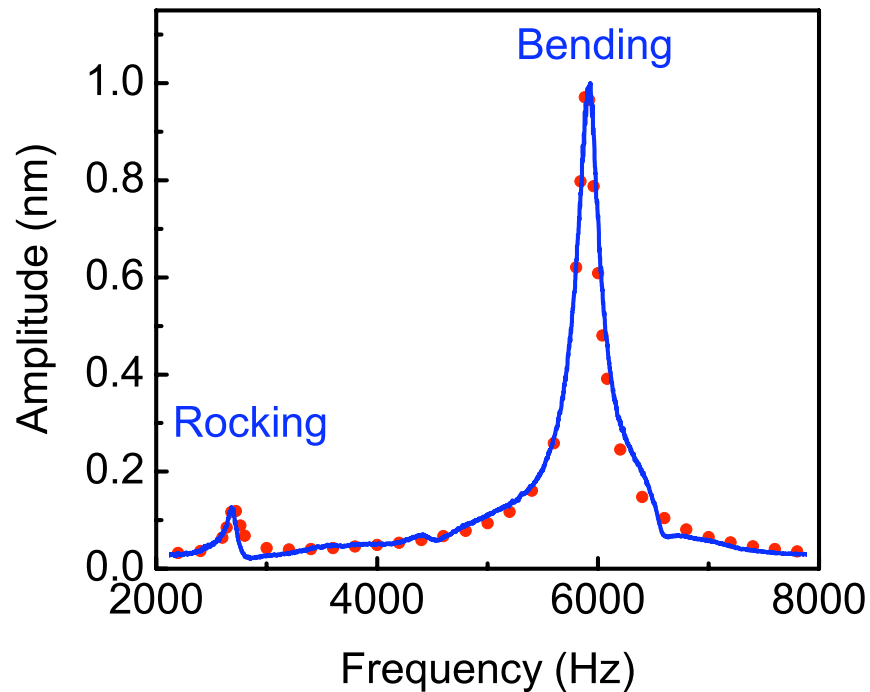


Figure 6.1: Frequency response of a FEM and fabricated device.

Since the various designs have only minor variations from the device presented in Figure 6.1, all the devices show a similar frequency response and presenting each device's response is not particularly informative. The frequency response evaluation is used extensively throughout the rest of the paper to discuss individual characteristics of the devices in general.

6.2 Directionality

As the purpose of this research is to develop a directional, sound sensor, the directional response is clearly of primary importance. The preliminary theory and investigation found that the directional dependence of the device should be seen only in the rocking mode due to the slight variation in phase between the two sides. This phase difference is amplified through the coupling between the two modes. By using a packaging scheme which allows the sound to impact the back side of the device, however, both modes are affected by the pressure-gradient effect discussed earlier and show an added *cosine* dependence on angle.

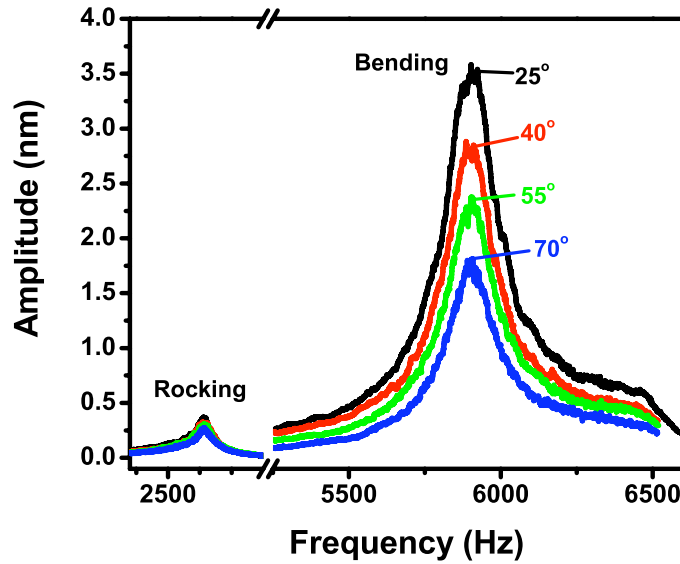


Figure 6.2: Experimental frequency response of a MEMS directional sound sensor with symmetric wings at various angles.

Figure 6.2 shows the measured frequency response of the sensor in Figure 4.7 at a set of incident angles using a laser vibrometer. As expected, the response at the rocking frequency was found to be relatively weak compared to that of at the bending frequency. In addition, the amplitude at the bending motion showed a *cosine* dependence as expected due to the pressure gradient, and the angular dependence of the two amplitudes are now given by [31]

$$\begin{aligned} A_r &\propto (\omega d/v_s) s P_0 \sin \theta \cos \theta \\ A_b &\propto s P_0 \cos \theta \end{aligned} \quad (6.1)$$

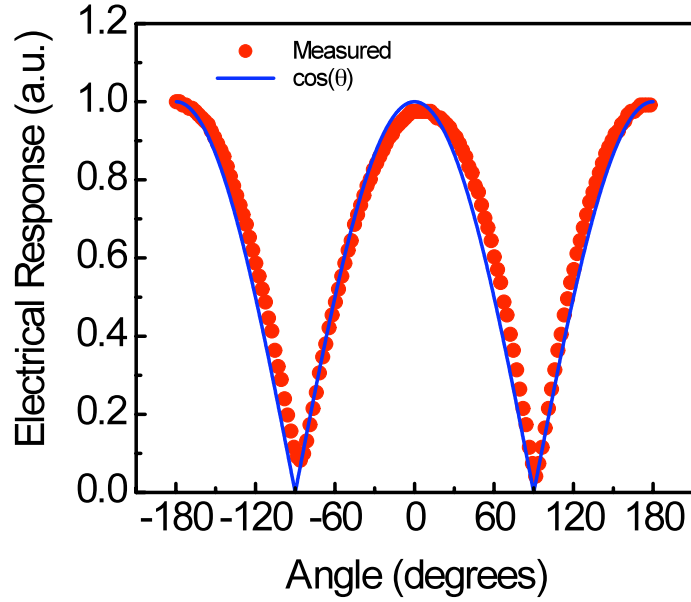


Figure 6.3: Experimental directional response (solid circles) of a MEMS directional sound sensor with symmetric wings. Solid line shows the $\cos \theta$ dependence.

In order to experimentally verify the directionality of the device, it was crucial to minimize or eliminate any reflections of the driven source wave. This was accomplished using the electronic readout system described in Chapter 5. The device was mounted on a motorized rotating pedestal in the acoustic anechoic chamber at the Naval Postgraduate School. The angular position of the device and signal amplitude were both measured remotely while being driven by a sine wave at the bending-mode frequency from approximately 3 m away. The results (also reported in [30] and [31]) are shown in Figure 6.3, along with a *cosine* curve. The amplitude at the rocking frequency is too small to be measured electronically due to limitations of the present electronic readout system.

6.3 Linearity

In the final implementation of the devices being developed in this research, determination of direction would be greatly simplified if the device responded linearly with sound pressure. To test the linearity of the device, it was driven by a sinusoidal signal (at the bending mode) with varying amplitude and the response was measured by laser vibrometer. The steady-state, root-mean-squared (rms) amplitude is shown as a function of sound pressure (as measured using the

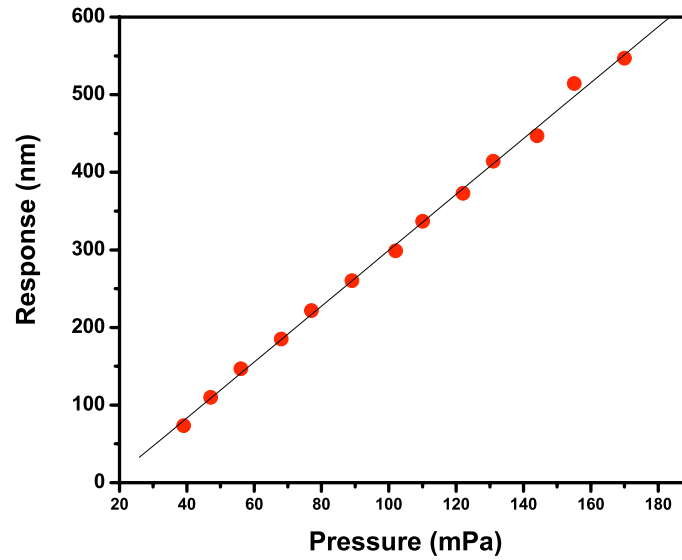


Figure 6.4: Amplitude versus pressure of device driven by a sine wave at its bending-mode frequency. Note that the device responds linearly with sound pressure in the tested range.

reference microphone) in Figure 6.4.

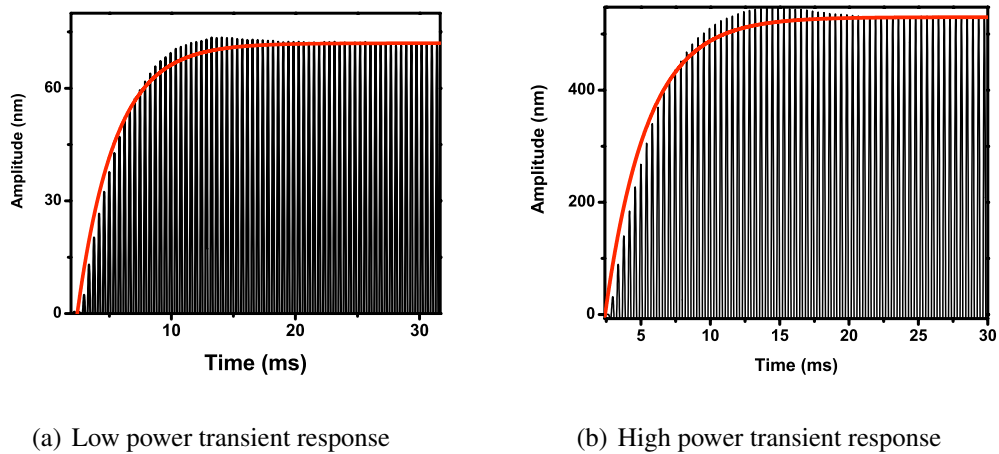


Figure 6.5: Transient response of device when first driven by sinusoidal signal with (a) 39 mPa and with (b) 170 mPa sound pressure. Note the time constant of the exponential amplitude growth is approximately 3 ms in both cases.

As the devices may ultimately be used with transient signals, it is also important to understand the impact of source amplitude on the transient response of the device which is primarily governed by the damping experienced by the device. The time constant of a damped oscillator is defined as the time it takes for the oscillator to decay from its steady-state amplitude by a factor of $1/e$, equivalent to C in Equation (3.15). This value was determined experimentally by plotting the rising edge of the device response when the acoustic signal is first radiated. The envelope of this curve is compared to a plot of $A_{max} \cdot (1 - e^{t/\tau})$ and varying τ until the best fit is achieved to extract the time constant.

Figures 6.5(a) and 6.5(b) show the transient response of the device to an incident sinusoidal signal at the bending-mode frequency with sound pressure amplitudes of 39 mPa and 170 mPa, respectively. Both signals show similar response when compared to a damped oscillator with a time constant, τ , of 3 ms. This comparison shows that steady-state amplitude is linearly dependent on amplitude while the rise-time is independent of amplitude, which will greatly simplify the signal calibration for future devices.

6.4 Damping

To investigate the impact of the comb fingers on damping, several device designs were compared; their dimensions are shown in Table 6.1. Maintaining the overall device structure as a control, the number of comb fingers was varied in each device and the peak widths and rise times were used to evaluate the amount of damping.

Table 6.1: Device dimensions used to compare effects of comb fingers on damping

Device	Wing width (μm)	Wing length (μm)	Bridge width (μm)	Comb fingers
1C	1000	750	80	125
1C+	1000	750	80	218
1NC	1000	750	80	0
2C	1000	990	240	125
2NC	1000	990	240	0
3C	2000	1250	300	250
3C+	2000	1250	300	500

Devices 2C and 2NC from Table 6.1 differ only in that 2C has comb fingers on the end of the device while the latter has none. When the frequency response of the two are compared (see Figure 6.6), the device with comb fingers shows a significant increase in bandwidth ($> 300\%$)

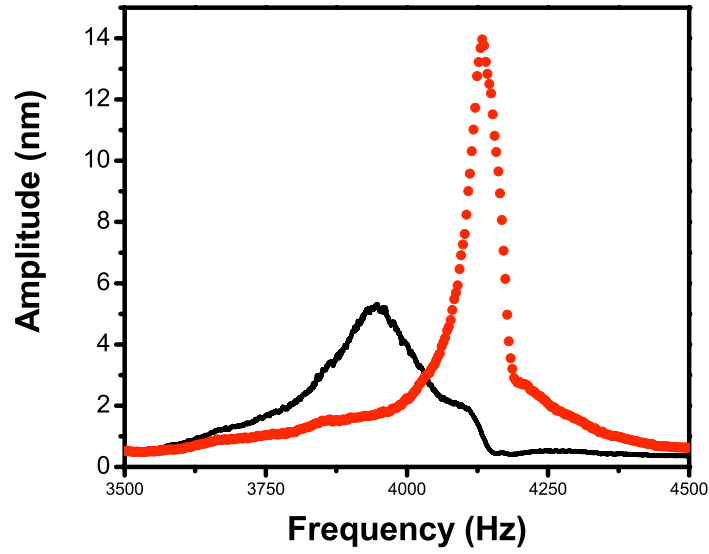


Figure 6.6: Frequency response of a rectangular-shaped device with comb fingers (black solid line) and a similar device without comb fingers (red broken line). The comb fingers greatly increase the damping causing a decreased resonant frequency and amplitude, but larger bandwidth.

as well as a decrease in amplitude, resonant frequency, and time constant (rise time) as given in Table 6.2.

Table 6.2: Comparison of two devices with identical dimensions except that one (2C) has comb fingers while the other does not.

Device	f_{bend} (Hz)	Amplitude (nm)	FWHM (Hz)	τ (ms)	Comb fingers
2C	4024	515	233	3.06	125
2NC	4123	1385	74	8.1	0

The effects of the comb fingers on device response speed can be most clearly seen in Figure 6.7 where the normalized device responses are shown for devices with and without comb fingers. The absolute response is shown in Figure 6.8.

The electrical noise floor of the device is determined by equating the thermal energy to the

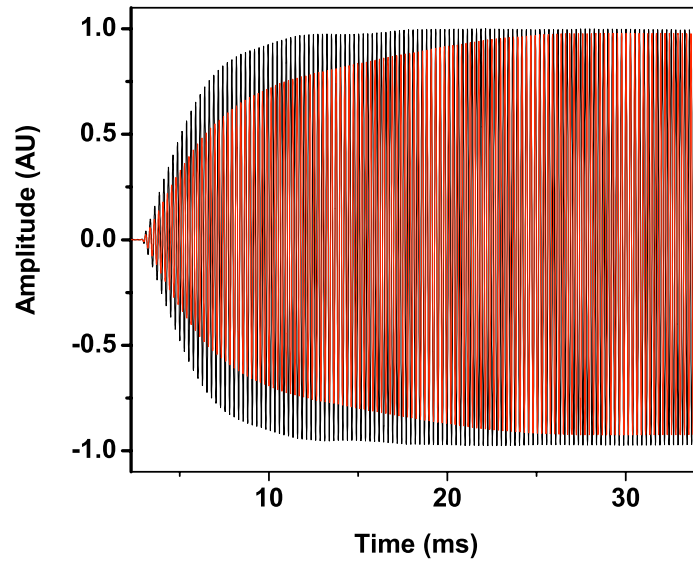


Figure 6.7: Normalized comparison of the rise-time of a device with comb fingers vs one with no comb fingers. The additional damping due to comb fingers causes that device to approach its steady-state more quickly.

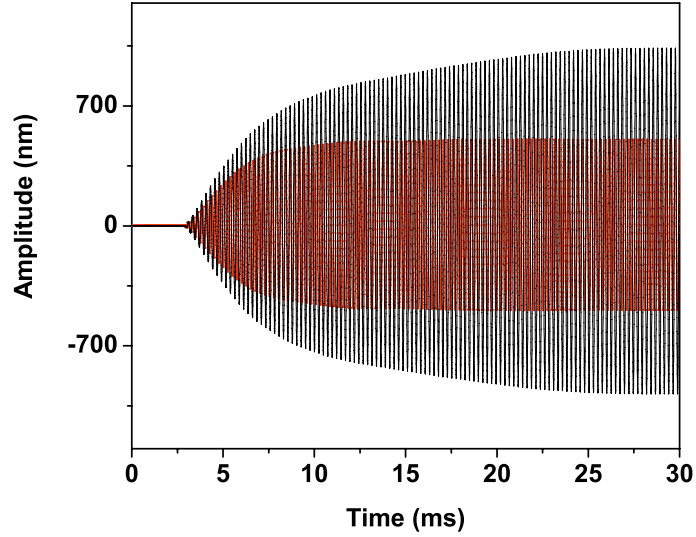


Figure 6.8: Absolute comparison of the transient response of a device with and without comb fingers.

electrostatic energy present in the capacitor[38], giving

$$E = \frac{CV^2}{2} = \frac{kT}{2}$$

where E is the energy, C the capacitance of the comb fingers, V the potential between the moving fingers and the fixed substrate fingers, k is Boltzmann's constant, and T is the temperature of the device. Solving for V gives the thermal noise-equivalent voltage, or

$$V = \sqrt{\frac{kT}{C}} \quad (6.2)$$

Therefore, designing additional comb fingers not only increases the electrical signal, but also decreases the noise floor of the system.

Given the reduction of vibration amplitude observed in the previous comparison between devices with and without comb fingers, it is important to know whether the reduction in mechanical response due to additional comb fingers would outweigh the increase in electrical signal. To that end, another comparison was made between two devices with a different number of comb fingers. Table 6.3 shows a comparison of two devices that both have comb fingers, but device 3C has them only on the ends of the wings while 3C+ has fingers on three sides of the wings. This doubles the number of comb fingers and, as seen in the table, the changes in mechanical response are insignificant as the resonant frequency and amplitude each change by less than 2%.

Table 6.3: Comparison of two devices with identical dimensions except that one (3C+) has more comb fingers than the other.

Device	f_{bend} (Hz)	Amplitude (nm)	FWHM (Hz)	τ (ms)	Comb fingers
3C	2480	415	77	4.1	250
3C+	2430	405	83	3.9	500

The physical explanation for the minimal effect of increasing the number of fingers is not entirely understood and will be the subject of future work, as a new design is currently in fabrication to test the relationship between the number of fingers and damping effects. One factor that certainly contributes is that the distance between the comb fingers is much less than the acoustic

penetration depth, δ_p , given by[39]

$$\delta_p = \sqrt{\frac{2\nu}{\omega}} \quad (6.3)$$

where ν is the viscosity of air. This value determines the velocity profile of the air as a function of distance from a rigid structure. With a penetration depth on the order of $30 \mu\text{m}$ and a finger separation of only $2 \mu\text{m}$, the comb finger array collectively adds to the effective surface area of the device and increases the force due to incident sound pressure. This increases the amplitude and counteracts the damping added by the comb fingers. A similar effect was studied in [40] regarding wing perforations and will be discussed in Section 6.5. Another potential cause of the described relationship is the fact that the additional comb fingers on device 3C+ are oriented perpendicular to the set of fingers on device 3C.

Table 6.4: Comparison of three devices with identical dimensions except for the number of comb fingers attached.

Device	$f_{bend}(\text{Hz})$	Amplitude (nm)	FWHM (Hz)	τ (ms)	Comb fingers
1NC	4135	1060	68	5.3	0
1C	4022	395	103	3.2	125
1C+	3948	505	103	3.0	218

Both of the relationships analyzed above are further supported by the data in Table 6.4 after analyzing a set of devices with no comb fingers, 125 comb fingers, and 218 comb fingers. The resonant frequency again decreases with the addition of comb fingers, as does the time constant. The amplitude difference between devices 1C and 1C+ are not suitable for a rigorous quantitative comparison because they are located at different sites on the chip (edge versus center), which impacts the device response as explained further in Section 6.6. This does not, however, invalidate the results for the resonant frequency or time constant comparison because neither are affected by sound pressure levels as shown in Section 6.3. It should also be noted that the number of additional fingers is greater in the Table 6.3 comparison than that in Table 6.4.

This section has shown that the effect of adding comb fingers to a design that originally has none greatly affects the device response, but once comb fingers are added to a design the response is minimally impacted by adding more comb fingers. Doubling the number of comb fingers does, however, roughly double the electrical output of the device as seen in Figure 6.9. This confirms that it is certainly desirable to design as many comb fingers into the device as possible if it is

going to be used for electronic readout.

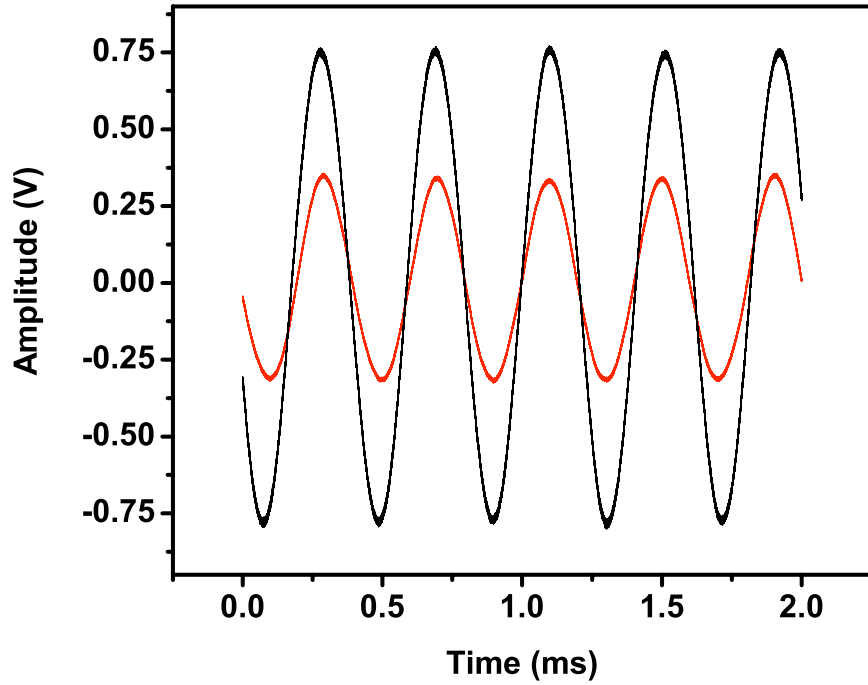


Figure 6.9: Amplitude vs. time of the measured electronic signal from two devices, one with approximately twice as many comb fingers as the other. Additional damping effects are minimal.

6.5 Perforated Wings

The first devices that were produced for this research were fabricated using PolyMUMPS process instead of SOIMUMPS and did not have the substrate removed beneath the device. In order to allow the wing to release from the substrate beneath it, the wing was perforated to allow the releasing agent to better penetrate the wing. In later iterations of the device, similar perforations, like those seen in Figure 6.10 were used as an additional design parameter to adjust the wing mass and increase the surface area.

As presented in Section 6.4, the acoustic penetration depth at the frequencies of interest in this project are on the order of $30\text{ }\mu\text{m}$. In order to minimize any reduction in effective driving force, the wing perforations should be designed well below this threshold. The first study of the effect

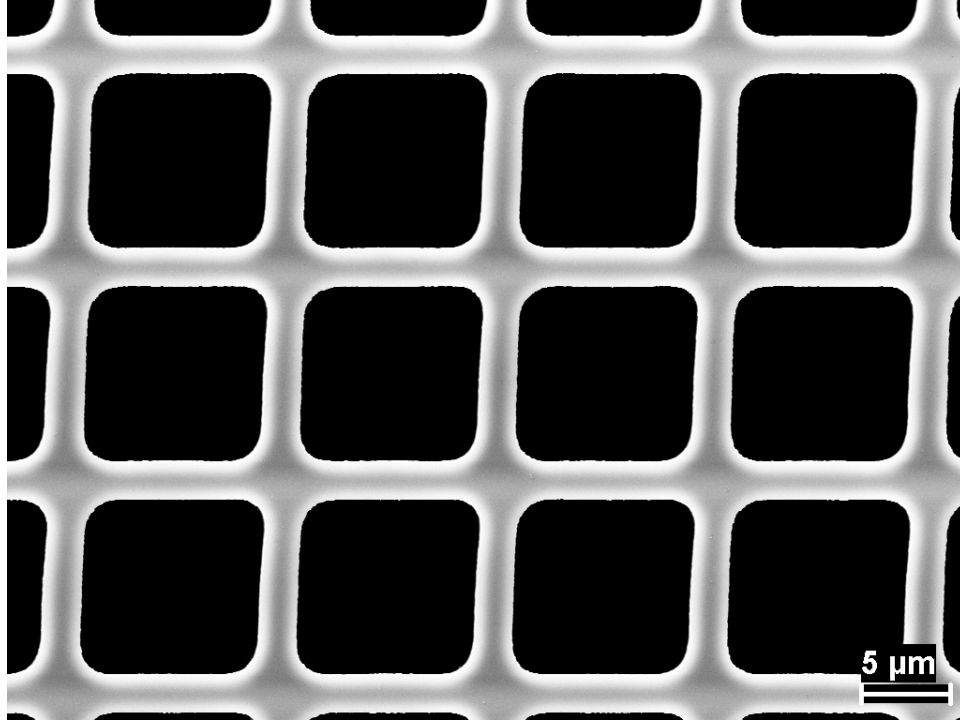


Figure 6.10: SEM image of device with $10\ \mu m$ square perforations.

of wing perforations for the reported devices was in [40]. The study compared two devices (4 and 6 from Generation 4, dimensions listed in the Appendix) that differ only in that $2\ \mu m$ perforations are etched throughout the wings of Device 4, while Device 6 has solid wings. That study showed that the decreased mass due to the perforations causes a slight increase in resonant frequency and broadening of the resonant peak.

This behavior was further tested using Device 3 (with $2\ \mu m$ perforations) and Device 4 (solid wing) from Generation 5 (seen in Figure 4.9). These devices differ from the previous study in that they also have comb finger capacitors on the end of each wing. One advantage to this particular comparison is that these two devices are exactly opposite each other on the chip, meaning that by inverting the chip, the two devices can be tested in the same relative position to eliminate any effects due to the surrounding SOI. As seen in Figure 6.11, the frequency response at resonance is virtually identical for both devices, with the perforated wing responding with a slightly decreased amplitude (by $\approx 12\%$) and increased bandwidth ($\approx 9\%$ change in the FWHM). The change due to damping is much smaller than that found in [40] likely because the comb fingers on the Gen 5 devices make the fractional damping change much smaller than with

the earlier (Gen 4) devices. Also, while the perforations were designed with a $2\ \mu\text{m}$ diameter, they are actually less than $1\ \mu\text{m}$ as seen in Figures 6.12(a) and 6.12(b).

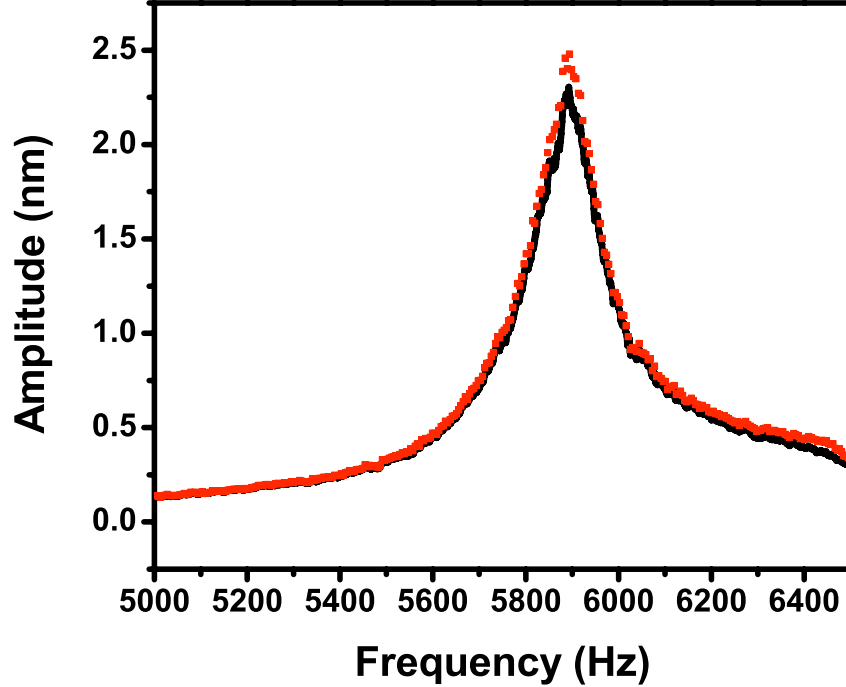


Figure 6.11: Frequency response of a device with solid wings (broken line) and a device with $2\ \mu\text{m}$ perforations throughout the wing. The perforated device shows a slightly reduced amplitude and increased bandwidth due to the additional damping.

While it is seen above that there is a minimal impact due to the $2\ \mu\text{m}$ holes, larger perforations have also been designed and tested. Specifically, devices 1 and 3 from Generation 6 were compared, which have $5\ \mu\text{m}$ and $10\ \mu\text{m}$ perforations, respectively. The devices were mounted in slightly different ways, so packaging effects preclude a comparison of the absolute response, but since it has already been shown that the damping coefficient is not affected by changes in effective pressure it is reasonable to compare the normalized responses for purposes of evaluating the damping effects of increased perforation dimensions. The two normalized responses are shown in Figure 6.13. The legs of Device 1 are 20% smaller than those of Device 3, but that primarily affects the rocking mode resonance and should have a minimal effect on the bending mode frequency. The frequency shift seen in Figure 6.13 is primarily due to the reduced mass of the wings with larger perforations. This frequency shift should impact the damping coefficient

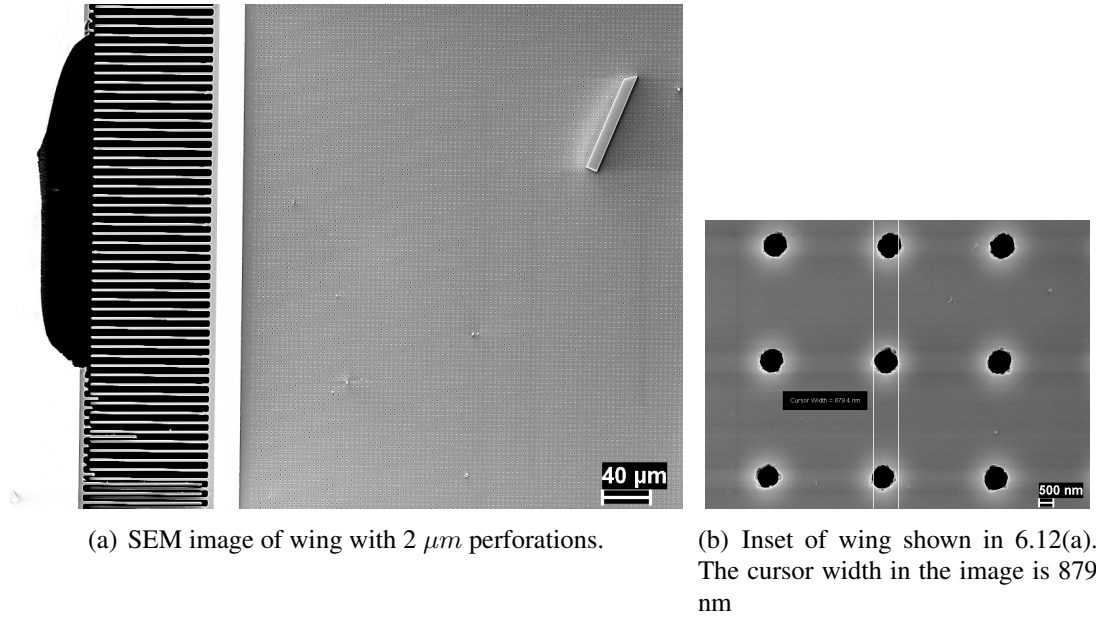


Figure 6.12: SEM images of device with with $2\ \mu\text{m}$ perforations.

by increasing it approximately 12%. The Full Width at Half Maximum (FWHM) of Devices 1 and 3 are 129 Hz and 389 Hz, respectively. After subtracting the impact due to the frequency change this yields a damping coefficient increase of approximately 270%, showing that adding holes with dimensions closer to the value of the penetration depth does have a significant impact on the damping.

6.6 Packaging Effects

To test the effects of the surrounding packaging, devices were tested (by laser vibrometry) with three different package dimensions. The (red) data labeled *Gen6* in Figure 6.14 was taken with a single device mounted on a SOIC package approximately 1 cm wide and yielded the smallest amplitude. Then a 2 cm baffle was placed around the SOIC amplitude approximately doubled (plotted in green). Finally, the amplitude of a different device (*Gen4*, plotted in blue) mounted on a 4 cm PGA socket was found to be approximately twice the amplitude of the 2 cm package.

Because the earlier iterations of the chip designs contained many devices, each device is situated in a different location on the chip. Given the above discussion regarding packaging effects, the site location of the device will have an impact on the response. If the device is located on the near edge of the chip or packaging, for example, it will experience less of a pressure-gradient

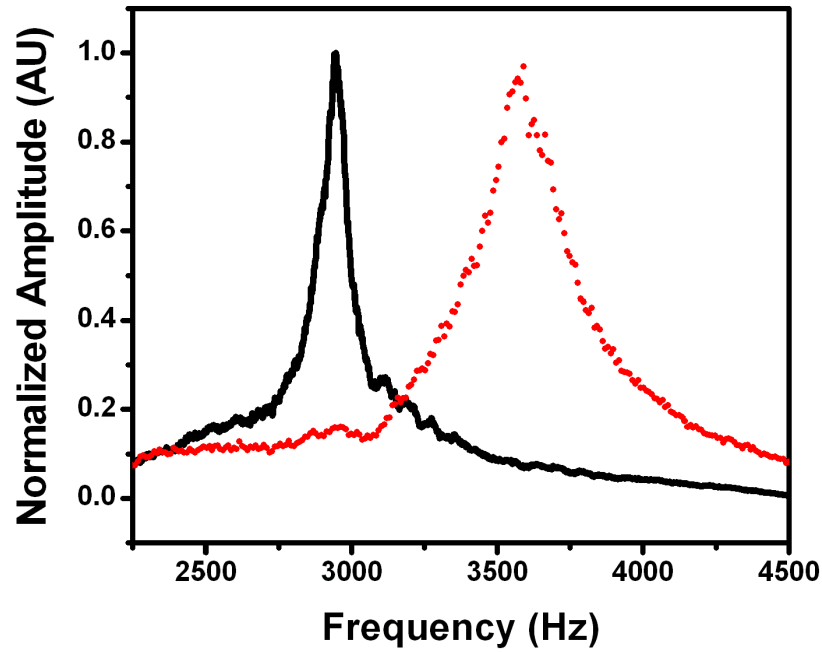


Figure 6.13: Frequency response of devices whose wings are etched with square perforations whose sides measure $5\ \mu\text{m}$ (solid line) and $10\ \mu\text{m}$ (broken line). Units are normalized to show that larger holes cause increased damping and a wider resonance peak.

from the diffraction path-length difference than would a device located at the center of the chip.

This effect was also noted during the testing reported in Section 6.5. While the presence of perforations certainly had the largest effect on device amplitude, inducing a 12% change, the side of the device also saw a difference in amplitude with the contralateral side responding with a 13% greater amplitude than the ipsilateral. This is the opposite of what is predicted by the simple mechanical theory, but is understandable when considering that the path length term in the pressure-gradient formula is slightly increased on the contralateral side.

While this presents a challenge when comparing multiple devices experimentally, it can be factored into the final packaging of a system to simplify discrimination of the sound source bearing by forcing a larger difference in response between the same angle on different sides. Current designs generally incorporate subdicing trenches so the individual device can be separated and mounted in the center of the package to aide in developmental testing.

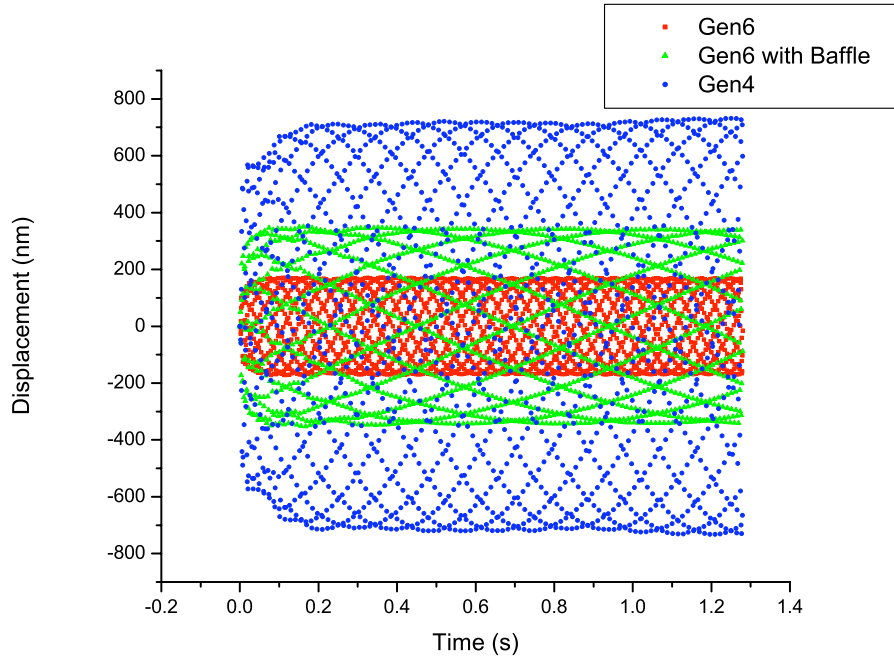


Figure 6.14: Comparison of device with several different packaging dimensions. The package sizes for the three samples were approximately 1 cm, 2 cm, and 4 cm with the largest amplitude occurring with the largest package.

6.7 Impulsive Sources

One of the primary goals of this research is to provide a technology that can be used as a passive sniper or gunshot location system that is small enough to be practically carried by individual soldiers. With current systems, the size and weight contribute to soldier fatigue and can interfere with agility needed during combat maneuvers and when taking enemy fire.

With the time constants of the devices reported here, it can take more than 10 ms to effectively reach a steady state response. With the goal of using the device for sniper detection, it is important to test the device response to impulsive or transient sounds like gunshots. The advantage of using the device for such signals is that an impulse-type sound is necessarily very broadband, which ensures there will be a significant component of the incident sound at one or both resonant frequencies of the device.

To test the response to these impulsive sounds, the device was driven with a digitized recording

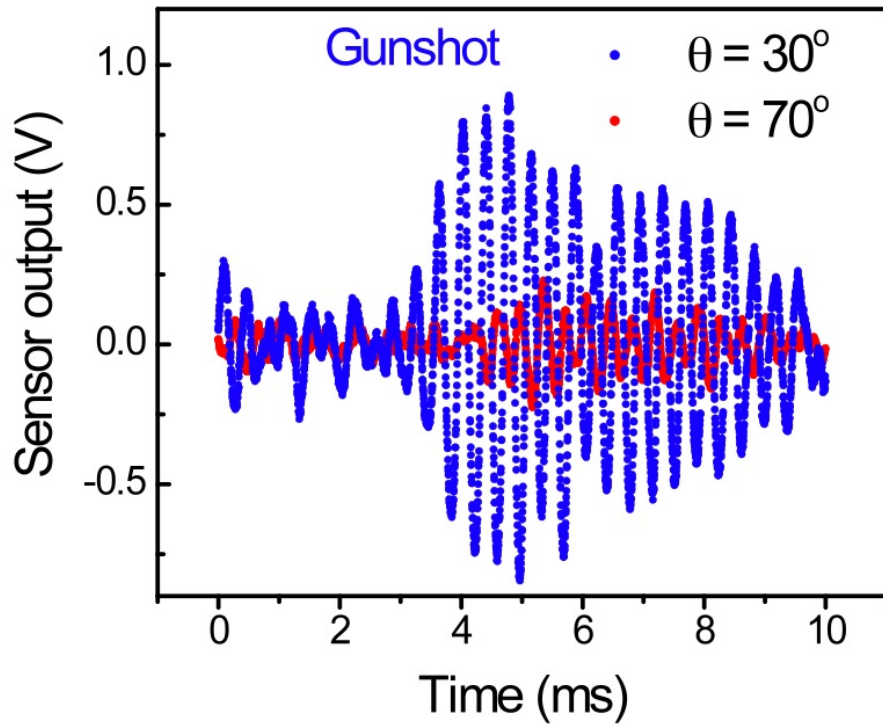


Figure 6.15: Experimental transient response of device to simulated (computer generated) gunshot sound from two different angles.

of a gunshot played through the laboratory setup (computer, amplifier and speaker) at various angles. As seen in Figure 6.15, using the MS3110 electronic readout described earlier the device output was recorded and, despite the short duration of the main acoustic impulse, the output from the readout IC was nearly 1V. As the angle increases from normal incidence, the signal envelope decreases as expected (see Figure 6.16). Signals of this strength are certainly large enough for even the simplest analog to digital conversion (ADC) circuits meaning this technology should be easily implementable using common embedded systems or systems-on-chip (SOC) hardware.

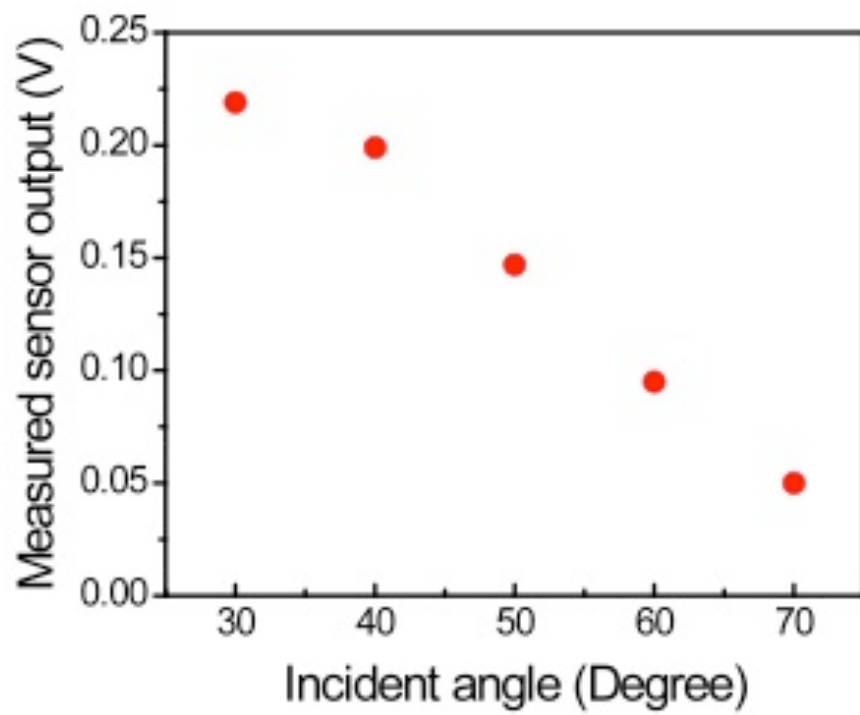


Figure 6.16: RMS amplitude of device in response to simulated (computer generated) gunshot sound from various angles.

THIS PAGE INTENTIONALLY LEFT BLANK

CHAPTER 7:

Dual Frequency Sensor

[Note: This chapter was also published in [41].]

As discussed earlier, the rocking motion is the result of a difference in acoustic pressure between the two sides of a device; namely the total effective rocking pressure, $P_r(t)$, is given by $P_i(t) - P_c(t)$, where P_i is the pressure on the ipsilateral or near side and P_c is the contralateral pressure on the side further from the sound source. The bending motion is driven, instead, by the sum of the two pressures: $P_b(t) = P_i(t) + P_c(t)$. This results in a bending amplitude that is much larger than that of the rocking mode.

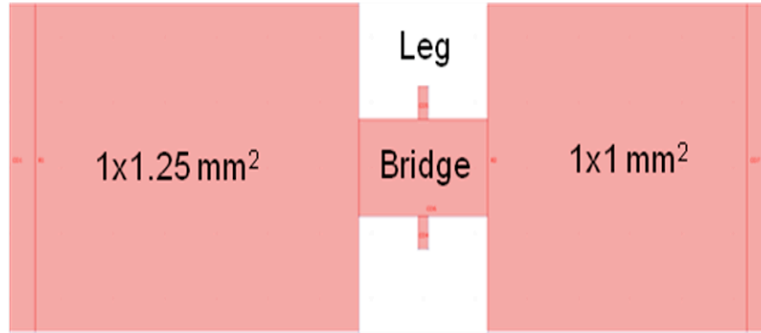


Figure 7.1: L-Edit footprint of the asymmetric design for dual-band detection

With a lateral separation between the two wings of roughly one millimeter (versus a wavelength of approximately 25 cm given a rocking mode resonance of 1.4 kHz), the phase difference between the two sides is approximately 1.4° in the rocking mode. This means that the pressure at the two wings is essentially in phase and causes the difference in pressure to be very small. Because the rocking mode amplitude is governed by this difference in pressure, the rocking mode is barely detectable above the noise floor as seen in the frequency response in Figure 6.2. If the areas of the two wings [s in Equations (6.2)] are not identical, however, the difference in area can cause a much greater difference in the effective force on each side and the amplitude at the rocking frequency is greatly increased. A finite element model was developed with asymmetric wings in COMSOL Multiphysics software and extensive simulation was conducted to optimize the design for fabrication. The new sensor consists of two wings with dimensions $1 \times 1 \text{ mm}^2$ and $1 \times 0.75 \text{ mm}^2$ that are connected to the substrate via two $100 \text{ }\mu\text{m}$ long and $40 \text{ }\mu\text{m}$ wide legs

(see Figure 7.1).

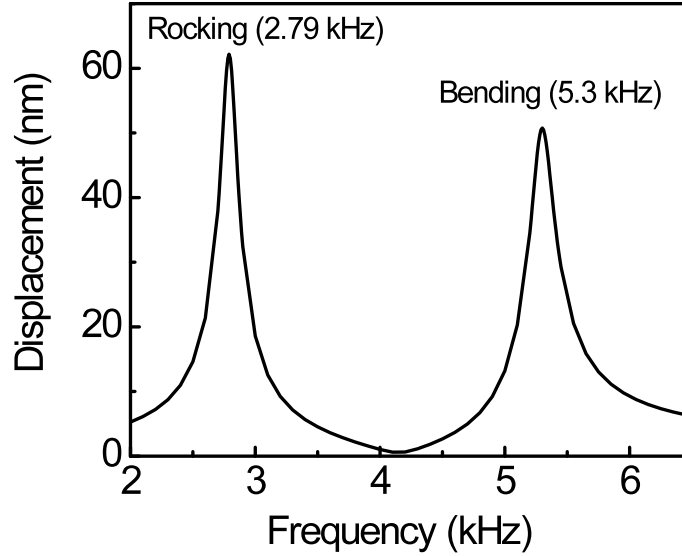


Figure 7.2: Simulated frequency response at normal incidence. The two resonant peaks are associated with rocking and bending modes of the sensor.

The frequency response of the sensor in Figure 7.1 was simulated using COMSOL and treating the incident sound as a plane wave to properly take in to account the diffraction effects which involves simultaneously solving structural and wave equations. The damping effects due to air drag were taken into account using the approach described in Chapter 6. Figure 7.2 shows the simulated frequency response of the sensor with asymmetric wings assuming the sound pressure magnitude at each frequency to be 1 Pa. The rocking and bending resonances were found at 2.79 kHz and 5.3 kHz, respectively. It can easily be seen that the use of the asymmetric wings greatly enhanced the amplitude of the rocking mode.

In addition to the frequency response, the amplitude at the rocking and bending frequencies as a function of incident angle of sound was also simulated as shown in Figure 7.3. The data shows that at both frequencies the amplitudes have the expected cosine dependence since the driving force is determined by $(s_1 - s_2)P_0 \cos \theta$, where s_1 and s_2 are the areas of the wings.

The optimized sensors were fabricated using the SOIMUMPS fabrication process as described previously. One of the devices (see Figure 7.4) was mounted on an open-backed dual in-line package (DIP) socket to minimize the interaction of the sound with the packaging. Using a

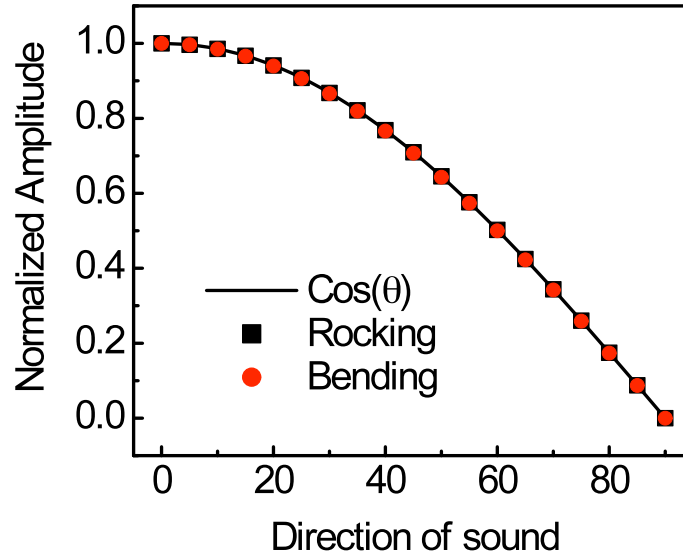


Figure 7.3: Simulated responses at rocking and bending frequencies as a function of incident angel of sound. The solid line shows cosine of the angle.

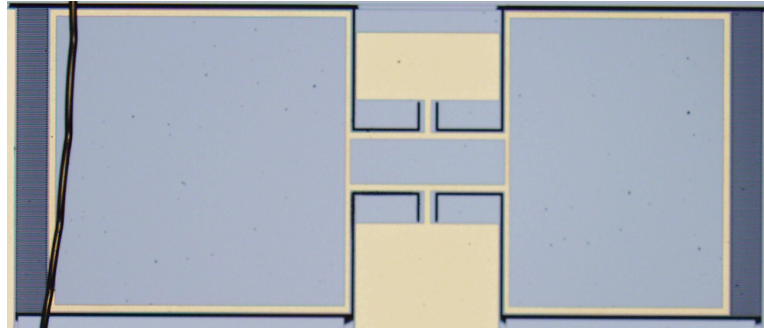


Figure 7.4: Photograph of fabricated asymmetric (dual-band) device

Polytec OFV-534 laser vibrometer and driving the device with a swept sine wave from 1 - 10 kHz, the mechanical frequency response was measured for a set of incident angles as shown in Figure 7.5. It can be seen that the amplitude of the measured frequency response is small compared to the simulation in Figure 2.7. This is primarily due to the fast frequency sweep used in the measurement compared to the time constant of the sensor (≈ 5 ms). The measured rocking and bending frequencies of the sensor were found to have nearly the same amplitudes with frequencies around 2.78 kHz and 5.29 kHz, respectively, and a bandwidth of about 100

Hz which is primarily due to viscous air damping (Figure 7.5). The measured frequencies are in close agreement with that obtained from COMSOL simulation results. In addition, amplitudes at the two frequencies decrease rapidly as the incident angle is increased. The detailed comparison with the expected cosine behavior requires measurements to be carried out in an anechoic chamber using the electronic readout.

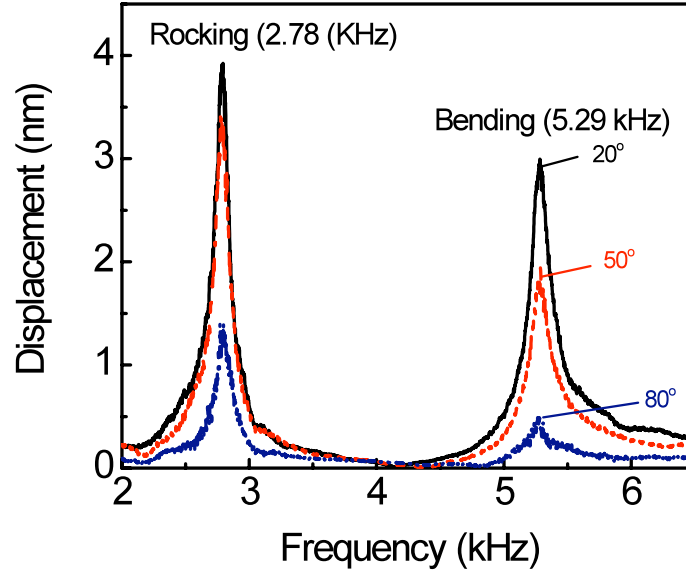


Figure 7.5: Experimental results showing frequency response at three different angles

The device presented in this section expands the potential for sensors modeled after the *Ormia ochracea* hearing system to allow acoustic direction finding with exceptional accuracy. In earlier designs, the response was limited to a single, narrow frequency band, but this device shows the possibility of extending the response into two bands while maintaining the directional sensitivity. The sensor provided spectral response in two bands with nearly the same amplitude. The simulated and measured frequency responses are found to be in close agreement which validates the approach used for simulation. By adding a second frequency to earlier designs, this design would allow the user to compare multiple frequencies to improve accuracy in finding the direction of wideband sources, or it could add the ability to distinguish between two specific sources.

CHAPTER 8:

Conclusion

Since the first recognition of the *Ormia ochracea*'s unique hearing structure it has been recognized as a potentially simple solution for overcoming the technical barrier of accurately determining sound source direction when the wavelength of interest far exceeds the dimensions of the sensor. In the current threat environment faced by the military, successfully developing a passive sensor weighing only a few ounces that could determine the direction of a sniper to within a few degrees would have a significant impact on the casualty rate of troops on patrol in hostile or potentially hostile territory.

The first step in the development of this sensor was to understand the physical phenomenon that allows the *Ormia* fly to locate its prey. While largely studied by Miles, et al., in [6], the background and biological structure are presented in Chapter 2. If incident sound carries some component within the resonant frequencies of the device, it will force the two wings of the device into motion. Because of their spatial proximity compared to the resonant wavelength, the structure is bent in-phase. As the angle of incidence increases, however, a minimal phase separation develops due to the time lag between the two sides and this net difference attempts to rock the device in an out-of-phase motion. This competition between the rocking and bending motion greatly magnifies the amplitude or phase difference observed in the response magnitude of the two wings and the sound source direction is extracted. This amplification of the phase and amplitude difference due to the coupling of the two modes is the single most important feature of the fly's structure that is to be emulated.

Chapters 3 and 4 present the specifics of the devices developed in the course of the research at the Naval Postgraduate School. Using capacitive comb fingers to read the response of the device allows a greatly simplified design and fabrication process that ultimately can save both time and cost to more quickly push the technology to the field for operational use. The use of a narrowband sensor at resonance has the added benefit that one can ideally use phase sensitive detection (as used in lock-in amplifiers) to detect signals that would otherwise be completely masked by noise. This also greatly simplifies the signal processing required by the supporting electronics. These readout systems are presented in Chapter 5.

The results of this research demonstrate the viability of using this novel design to perform

acoustic orientation on the millimeter scale. Typical devices yield about one micron of displacement under an incident sound pressure level of approximately 75 dB *re* 20 μ Pa. This, in turn, yields nearly 1 V_{pp} using the Irvine Sensors capacitive readout IC, which is easily readable with even the simplest analog processing electronics. It has been shown to respond to high intensity, impulsive sounds, as well as continuous-wave sources. The remaining results focused on understanding the various device parameters such as comb fingers and wing perforations on the resulting mechanical performance so they can be factored into future designs to achieve the desired results. The relative wing displacements were also found to be significantly impacted by the surrounding packaging and operational devices will certainly need to be adequately calibrated in their final form, but there is now a solid understanding of the factors that feed into the device response.

The next steps of this research are necessarily an improved readout technique that can be monolithically fabricated with the device to minimize stray capacitance and further reduce the final form of the sensor. Because of the narrowband nature of the structure, the phase sensitive detection approach demonstrated with the lock-in amplifier will likely provide the most compact, noise-resistant solution and ultimately the most soldier-friendly device possible to help save lives, and minimize the effectiveness of enemy snipers.

Appendix

This appendix provides the dimensions of individual devices that have been fabricated. All dimensions listed are in micrometers (μm).

Table A.1: Generation 4

Device	Wing	Bridge	Leg	Finger	Gap	Hole	Fingers (per side)	Orientation
1	1000 x 750	80 x 500	45 x 75	2 x 100	2	0	125	Bowtie
2	1000 x 750	80 x 500	45 x 75	2 x 100	2	0	218	Bowtie
3	1000 x 990	2*40 x 500	45 x 75	2 x 100	2	0	125	Rectangle
4	1000 x 750	100 x 500	45 x 75	0 x 0	0	2	0	Bowtie
5	1000 x 750	100 x 500	45 x 75	0 x 0	0	0	0	Bowtie
6	1000 x 750	100 x 500	45 x 75	0 x 0	0	0	0	Bowtie
7	1000 x 990	2*40 x 500	45 x 75	0 x 0	0	0	0	Rectangle
8	1000 x 750	80 x 500	45 x 75	0 x 0	0	0	0	Bowtie
9	1000 x 990	2*50 x 500	45 x 75	0 x 0	0	0	0	Rectangle
10	1000 x 750	100 x 500	45 x 75	2 x 100	2	0	125	Bowtie
11	1000 x 750	100 x 500	45 x 75	2 x 100	2	0	218	Bowtie
12	1000 x 990	100 x 500	45 x 75	2 x 100	2	0	125	Bowtie

Table A.2: Generation 5 - Bowtie shape, 125 fingers/side and 2 μm pitch.

Device	Wing size	Bridge size	Leg size	Finger size	Hole side
1	1000 x 1250	600 x 500	40 x 100	2 x 100	5
2	1000 x 875	400 x 500	50 x 100	2 x 100	0
3	1000 x 1000	500 x 500	50 x 95	2 x 100	2
4	1000 x 1000	500 x 500	50 x 95	2 x 100	0
5	1000 x 875	400 x 500	50 x 100	2 x 100	0
6	1000 x 875	400 x 500	50 x 100	2 x 100	2
7	1000 x 1250	500 x 500	50 x 95	2 x 100	10

Table A.3: Generation 6 - Bowtie shape, 125 fingers/side and 2 μm pitch.

Device	Wing	Bridge	Leg	Finger	Hole side	Notes
1	1000 x 1250	300 x 500	40 x 100	2 x 100	5	Asymmetric Asymmetric
2	1000 x 1000	200 x 500	50 x 100	2 x 100	0	
2a	1000 x 750					
3	1000 x 1250	300 x 500	50 x 100	2 x 100	10	
4	1000 x 1000	200 x 480	50 x 100	2 x 100	2	

Table A.4: Generation 8 - 10 μm layer. All bowtie shape.

Device	Wing	Bridge	Leg	Finger	Hole	Fingers
1	1000 x 1250	300 x 475	40 x 100	2 x 100	5	125
2	2000 x 1250	300 x 500	40 x 100	2 x 100	0	250
3	2000 x 1250	300 x 500	40 x 100	2 x 100	0	500
4	1500 x 1250	300 x 500	40 x 100	2 x 100	0	187

REFERENCES

- [1] N. H. Fletcher. *Acoustic systems in biology*. Oxford University Press, New York, Jan 1992.
- [2] W. Cade. Acoustically orienting parasitoids: fly phonotaxis to cricket song, *Science*, **190**(4221), pp. 1312–1313 (Dec 1975).
- [3] D. Robert, J. Amoroso, and R. Hoy. The evolutionary convergence of hearing in a parasitoid fly and its cricket host. *Science*, **258**(5085), pp. 1135–1137 (Nov 1992).
- [4] A. Mason, M. Oshinsky, and R. Hoy. Hyperacute directional hearing in a microscale auditory system. *Nature*, **410**, pp.686–690 (Apr 2001).
- [5] M. Akcakaya and A. Nehorai. Performance analysis of the *Ormia ochracea*'s coupled ears. *J Acoust Soc Am*, **124**(4), pp.2100–2105 (Oct 2008).
- [6] R. Miles, D. Robert, and R. Hoy. Mechanically coupled ears for directional hearing in the parasitoid fly *ormia ochracea*. *J Acoust Soc Am*, **98**(6), pp.3059–3070 (Dec 1995).
- [7] D. Robert, R. N. Miles, and R. R. Hoy. Directional hearing by mechanical coupling in the parasitoid fly *ormia ochracea*. *J Comp Physiol A*, **179**(1), pp.29–44 (Jan 1996).
- [8] H. Liu, Z. Chen, and M. Yu. Biology-inspired acoustic sensors for sound source localization. *Proc of SPIE*, **6932**(2Y), pp.1–8 (2008).
- [9] R. Miles, Q. Su, W. Cui, M. Shetye, and F. Degertekin. A low-noise differential microphone inspired by the ears of the parasitoid fly *ormia ochracea*. *J Acoust Soc Am*, **125**(4) pp.2013–2026 (Apr 2009).
- [10] A. Saito, N. Ono, and S. Ando. Micro gimbal diaphragm for sound source localization with mimicking *Ormia Ochracea*. *Proc of the 41st SICE Annual Conference, Osaka, Japan*, **4**, pp.2159–2162 (Jul 2002).
- [11] K. Yoo, C. Gibbons, Q. T. Su, R. N. Miles, N. C. Tien. Fabrication of biomimetic 3-d structured diaphragms. *Sensors and Actuators A: Physical*, **97-98**(3), pp.448–456 (Apr 2002).
- [12] W. Cui, B. Bicen, N. Hall, S. A. Jones, F. L. Degertekin, and R. N. Miles. Optical sensing in a directional MEMS microphone inspired by the ears of the parasitoid fly, *Ormia ochracea*. *Proc of the 19th IEEE Intl Conf on Micro Electro Mech Sys, Istanbul, Turkey*, pp.614–617 (Jan 2006).
- [13] E. Macaulay, W. Hartmann, and B. Rakerd. The acoustical bright spot and mislocalization of tones by human listeners. *J Acoust Soc Am*, **127**(3), pp.1440–1449 (Jan 2010).
- [14] F. Whightman and D. Kistler. The dominant role of low-frequency interaural time differences in sound localization. *J Acoust Soc Am*, **91**(3), pp.1648–1661 (Mar 1992).
- [15] A. Mills. On the minimum audible angle. *J Acoust Soc Am*, **30**(4), pp.237–246 (Apr 1958).

- [16] Jpaur. A gravid female ormia ochracea resting on a fingernail. Licensed under CC-BY-SA-3.0 (<http://creativecommons.org/licenses/by-sa/3.0/deed.en>), Jan 2010. Retrieved 5/22/2011. [http://commons.wikimedia.org/wiki/File:Ormia_ochracea_\(gravid_female\).jpg](http://commons.wikimedia.org/wiki/File:Ormia_ochracea_(gravid_female).jpg).
- [17] A. Mörchen, J. Rheinlaender, and J. Schwartzkopff. Latency shift in insect auditory nerve fibers. *Naturwissenschaften*, **65**, pp.656–657 (1978).
- [18] T. Walker. Monitoring the flights of field crickets (*gryllus* spp.) and a tachinid fly (*euphasiopteryx ochracea*) in North Florida. *Fla Entomol*, **69**(4), pp.678–685 (Dec 1986).
- [19] M. Oshinsky and R. Hoy. Physiology of the auditory afferents in an acoustic parasitoid fly. *J Neurosci*, **22**(16), pp.7254–7263 (Aug 2002).
- [20] D. Robert, R. S. Edgecomb, M. P. Read, and R. R. Hoy. Tympanal hearing in tachinid flies (Diptera, Tachinidae, Ormiini): The comparative morphology of an innovation. *Cell Tissue Res*, **284**(3), pp.435–448 (1996).
- [21] T. J. Shivok. MEMS POLYMUMPS-based miniature microphone for directional sound sensing. Master’s thesis, Naval Postgraduate School, Sep 2007.
- [22] B. Arthur and R. Hoy. The ability of the parasitoid fly *Ormia ochracea* to distinguish sounds in the vertical plane. *J Acoust Soc Am*, **120**(3), pp.1546–1549 (Sep 2006).
- [23] K. Yoo, Q. Su, R. Miles, and N. Tien. Biomimetic direction-sensitive micromachined diaphragm for ultrasonic transducers. *Proc of the 2001 IEEE Ultrasonics Symposium, Atlanta, GA*, pp.887–890 (2001).
- [24] H. J. Liu, M. Yu, and X. M. Zhang. Biomimetic optical directional microphone with structurally coupled diaphragms. *Appl. Phys. Lett.*, **93**(24)3902 pp.1–3 (Dec 2008).
- [25] D. Grevenitis. Effects of substrate on response of mems directional sound sensor. Master’s thesis, Naval Postgraduate School, 2010.
- [26] L. D. Landau and E. M. Lifshitz. *Mechanics*, volume 1 of *Course of Theoretical Physics*. Elsevier Butterworth-Heinemann, Oxford, 3rd edition, 1976.
- [27] H. Hosaka, K. Itao, and S. Kuroda. Damping characteristics of beam-shaped micro-oscillators. *Sensors and Actuators A: Physical*, **49**, pp.87–95 (1995).
- [28] W. Zhang and K. Turner. Frequency dependent fluid damping of micro/nano flexural resonators: Experiment, model and analysis. *Sensors and Actuators A: Physical*, **134**, pp.594–599 (2007).
- [29] C. Liu. *Foundations of MEMS*. Illinois ECE Series. Pearson Education, Inc, Upper Saddle River, NJ, 2006.
- [30] K. Simsek. Developing a capacitance readout circuitry for a directional MEMS sound sensor and sound source localization in a sensor network environment. Master’s thesis, Naval Postgraduate School, Jun 2009.

- [31] M. Touse, J. Sinibaldi, K. Simsek, J. Catterlin, and G. Karunasiri. Fabrication of a microelectromechanical directional sound sensor with electronic readout using comb fingers. *Appl Phys Lett*, **96**(17)3701, pp.1–3 (Apr 2010).
- [32] S. Harrison. Free field modeling of a MEMS-based pressure gradient microphone. Master’s thesis, Naval Postgraduate School, Jan 2009.
- [33] D. Homentcovschi and R. Miles. Viscous microstructural dampers with aligned holes: Design procedure including the edge correction. *J Acoust Soc Am*, **122**(3), pp.1556–1567 (Sep 2007).
- [34] L. E. Kinsler, A. R. Frey, A. B. Coppens, and J. V. Sanders. *Fundamentals of Acoustics*. John Wiley & Sons, Inc., 4th edition, 2000.
- [35] A. Cowen, G. Hames, D. Monk, S. Wilcenski, and B. Hardy. *SOIMUMPS Design Handbook v.7.0*. Technical report, MEMSCAP Inc., 2011.
- [36] M. Touse. Demonstration of a near and mid-infrared detector using multiple step quantum wells. Master’s thesis, Naval Postgraduate School, Sep 2003.
- [37] Irvine Sensors Corporation, Costa Mesa, California. *MS3110 Universal Capacitive Readout IC Manual*, May 2004.
- [38] S. Senturia. *Microsystem design*. Kluwer Academic Publishers, 2001.
- [39] L. D. Landau and E. M. Lifshitz. *Fluid Mechanics*, Volume 6 of *Course of Theoretical Physics*. Butterworth-Heinemann, Oxford, 2nd edition, 1987.
- [40] N. Muamad. Characterization of a MEMS directional microphone with solid and perforated wings. Master’s thesis, Naval Postgraduate School, Jan 2009.
- [41] M. Touse, J. Sinibaldi, and G. Karunasiri. MEMS directional sound sensor with simultaneous detection of two frequency bands. *Proc of the 9th IEEE Conf on Sensors, 2010, Waikoloa, HI*, pp.2422–2425 (2010).

THIS PAGE INTENTIONALLY LEFT BLANK

Initial Distribution List

1. Defense Technical Information Center
Ft. Belvoir, Virginia
2. Dudley Knox Library
Naval Postgraduate School
Monterey, California
3. Professor Gamani Karunasiri
Naval Postgraduate School
Monterey, California